



UNIVERSITÄT PADERBORN
Die Universität der Informationsgesellschaft

Quantum Detector Tomography of Superconducting Detector Arrays

Master Thesis

in Physics

in Partial Fulfillment of the Requirements for the Degree of
Master of Science

by

TIMON SCHAPELER

submitted to

Jun.-Prof. Dr. Tim J. Bartley

and

Prof. Dr. Torsten Meier

Paderborn, September 4, 2020

Contents

1	Introduction	1
2	Background	3
2.1	Superconducting Nanowire Single-Photon Detector	3
2.1.1	General Introduction	3
2.1.2	Operating Principle	3
2.1.3	Detector Characteristics	5
2.2	Quantum Detector Tomography	7
2.2.1	General Introduction	7
2.2.2	POVM Formalism	8
2.2.3	Photon-Number Resolving Detectors	8
2.2.4	Optimization	11
2.2.5	Theoretical POVMs	11
2.2.6	Detector Wigner Functions	14
3	Input State Calibration	15
3.1	Experimental Setup	15
3.2	Analysis	16
3.3	Second-Order Correlation Function	18
4	Detector Tomography: 4-Pixel Detector	21
4.1	Experimental Setup	21
4.2	Analysis	24
4.2.1	Coherent Input State Matrix	25
4.2.2	Measurement Statistics Matrix	26
4.2.3	POVM Reconstruction	27
4.3	Results	27
4.3.1	Reconstructed POVM Elements	27
4.3.2	Efficiency	29
4.3.3	Dark-Count Probability	30
4.3.4	Cross-Talk Probability	32
4.3.5	Detector Wigner Functions	34
4.3.6	Convergence and Sanity Check	35
5	Detector Tomography: 4-Bin Detector	39
5.1	Experimental Setup	39
5.2	Analysis	40
5.2.1	Coherent Input State Matrix	40

5.2.2	Measurement Statistics Matrix	41
5.2.3	POVM Reconstruction	43
5.3	Results	43
6	Scalability of Detector Tomography	47
6.1	Introduction: Loop-Detector Design	47
6.2	Simulation	48
6.2.1	Matrix-Construction	48
6.2.2	POVM Reconstruction	49
6.3	Experiment	50
6.3.1	Experimental Setup	50
6.3.2	Analysis	52
6.3.3	Results	54
7	Conclusion and Outlook	57
8	Bibliography	61
A	Appendix	67

Recent advances in quantum computation [1], and quantum communication and information systems [2–4] have shown how much quantum based technologies have evolved. In this age, online security especially secure data communication is of great importance to protect two parties from an unwanted listener. Light or, to be more precise single photons are ideal long-distance information carriers due to high transmission speed, large information capacity per particle and robustness to dephasing [2].

The choice of photons opens up the need for efficient single-photon detectors. First introduced by Gol'tsman et al. [5] and now one of the most prominent detectors are superconducting nanowire single-photon detectors (SNSPDs). They inherit low noise, high timing resolution and a near unity efficiency, especially for the telecommunication wavelength [6–10]. SNSPDs are click-detectors, which respond with an output signal if at least one photon is incident, therefore, they typically do not resolve the number of incident photons. Since 2001, when the principle of these detectors was first shown, many groups invested their effort to expand the areas of application of SNSPDs. The development of detector arrays [11–22] and advances in read-out techniques [23–29] enabled e.g. quasi-photon-number resolution in photon counting experiments, utilizing either the intrinsic properties of the detectors [30–32] or spatial or temporal multiplexing schemes [33, 34]. Furthermore, SNSPDs are useful for single-photon imaging [18, 35, 36], deep-space communication [37] and potentially dark matter detection [38].

As the possible applications for single-photon detectors, particularly SNSPDs and arrays of such, increase, a precise characterization is important. One approach relies on modeling a detector. However, this requires knowledge of the detector's figures of merit, such as efficiency, dark-count rate or spectral sensitivity and also their working principle [39]. Another approach, which will yield a quantum mechanical description of the device, is quantum detector tomography. Moreover, quantum detector tomography will fully characterize the functioning of the device without any prior knowledge about the working principle or type of detector. This is done, by observing the measurement outcomes of a detector in response to the known input states and afterwards reconstructing the so called positive operator valued measure (POVM) operators [39]. These POVM operators of the detector are equivalent to density operators of quantum states of light and can be seen as probabilities of different detector outcomes occurring given a specific number of incident photons.

Since 2008, when Lundeen et al. first presented the realization of detector tomography [40], it has been applied to avalanche photodiodes [41, 42], SNSPDs [33], single-photon energy resolving transition edge sensors [43] and further detection schemes [44, 45]. However, it has not yet been applied to spatial arrays of SNSPDs.

Part of this thesis is aimed at the applicability of quantum detector tomography on a 2×2 spatial array of SNSPDs (a 4-pixel SNSPD). Furthermore, this work will present which information the POVM operators can yield about the detector e.g. the efficiency, dark-count probability, cross-talk probability between pixels of the multi-pixel device [46–52] and a visualization of detection outcomes using Wigner functions. This will show the advantages of detector tomography compared to other characterization techniques such as model-based techniques [48, 53] or individually characterizing figures of merit. One well-designed experiment in combination with the tomographic reconstruction of the POVM operators of the device will yield a full description of the detector, including the previously mentioned figures of merit.

The size of SNSPD arrays increased from merely two pixels all the way to a kilopixel device [11, 17, 18, 22]. It is desirable to apply detector tomography to these large detector arrays, as it characterizes the device as a whole, rather than each pixel separately, which becomes unreasonable with an increasing array size. Hence, demonstrating the scalability of this technique is of great importance. Therefore, quantum detector tomography is applied to a simulation, as well as an experimental measurement of a non-saturable time-multiplexed loop-detector design [34] with a variable number of outcomes. Not only does this device enable the measurement of single photons but also of large photonic states making it an ideal candidate to test the general technique and scalability of quantum detector tomography.

2.1 Superconducting Nanowire Single-Photon Detector

This chapter will provide a brief introduction to superconducting nanowire single-photon detectors (SNSPDs). Although quantum detector tomography does not require any preliminary assumptions about the detector under test, as it treats the device as a black-box, a general knowledge about the detector will be useful.

2.1.1 General Introduction

Typical SNSPDs consist of nanowires of a superconducting material with ≤ 10 nm thickness and ≤ 200 nm width. These nanowires are commonly patterned into a meander structure (Fig. 2.1(a)) to ensure a larger active area, which increases the probability of photons impinging onto the nanowire. As the name suggests, SNSPDs make use of superconductivity to detect photons. This is generally accompanied by higher cost and engineering effort, however, will provide a strong reduction of noise processes making the detector more reliable [39]. Depending on the material of the wire, different operating temperatures have to be reached. Niobium nitride (NbN) was the first used material [5] with a superconducting transition temperature of 4 K. Smaller superconducting gap energy materials, such as tungsten silicide (WSi) have improved sensitivity for longer wavelength, especially at 1550 nm, at the cost of a lower operating temperature of below 1 K. Other materials e.g. niobium titanium nitride (NbTiN), molybdenum silicide (MoSi) or magnesium diboride (MgB_2) have also been used [6, 54].

2.1.2 Operating Principle

The detector is operated below its superconducting transition temperature, also called critical temperature, T_c and direct current biased below its critical current density J_c , to maintain the superconductive state (Fig. 2.1(b)(i)). The energy of a single photon is sufficient to excite hundreds of quasiparticles in the superconducting material, resulting in the formation of a localized hotspot (Fig. 2.1(b)(ii)). The hotspot, now being resistive, forces the supercurrent to flow around it, leading to an increasing current density at the edge of the nanowire. Since the wire is very narrow, the critical current density J_c can be exceeded, if the current bias I_{bias} is sufficiently large. As a result a resistive barrier will be formed across the width of the wire (Fig. 2.1(b)(iii-iv)) [5]. Subsequent Joule heating, a heating effect caused by current flowing through a resistive wire, assists the growth of

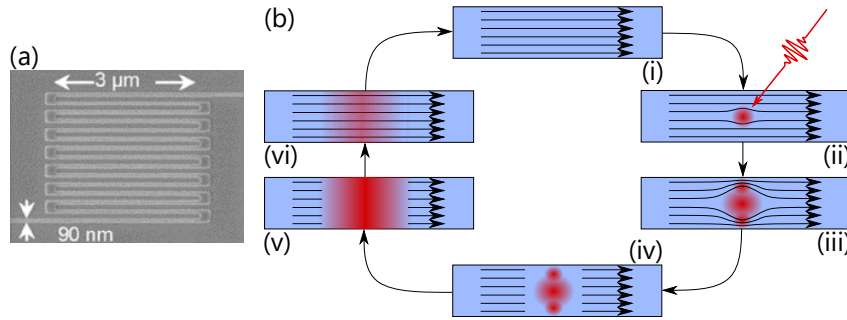


Figure 2.1: (a) Top-down scanning electron micrograph of a typical SNSPD meander structure [39]. (b) Schematic illustration of the detection mechanism of an SNSPD. (i) Current biased superconducting nanowire maintained below critical current and temperature. (ii) Formation of a resistive region (hotspot) due to photon absorption. (iii) Current density exceeds the critical value, as the current flows around the hotspot. (iv) Formation of a resistive barrier. (v) Joule heating leads to growth of the barrier along the length of the wire, entirely blocking the current flow and a measurable output pulse is created across the load impedance. (vi) Resistive region subsides due to constant cooling of the wire, restoring the superconductive state. (adapted from [6]).

the resistive region (Fig. 2.1(b)(v)) along the length of the wire [55]. This barrier blocks the current flow entirely and the bias current gets diverted into a parallel load impedance (Fig. 2.2(a)), causing a measurable voltage pulse (Fig. 2.2(b)), also referred to as a “click”. At this point, the detector is not susceptible to subsequent photons impinging, as no current is flowing through the nanowire. Typical dead times of SNSPDs are in the range of a few nanoseconds to tens of nanoseconds [39]. Due to constant cooling of the device, using a cryostat, the resistive region subsides (Fig. 2.1(b)(vi)). Once the superconducting state of the nanowire is restored, the detector is ready to detect photons again.

The detection operation was explained for a general (single-pixel) SNSPD. As mentioned in Chapter 1, arrays of SNSPDs, also called multi-pixel SNSPDs, exist. However, the described detection mechanism also applies to these devices. For multi-pixel detectors that are electrically wired in series (Fig. 2.3(a)), the amplitude of the output voltage pulse scales linearly with the sum of the pixels that fire. The outcomes of multi-pixel SNSPDs are often called n -click events. A 4-pixel detector has five possible outcomes, ranging from “0-clicks” or “no-clicks” to “at least 4-clicks”, where “at least” indicates that the detector can not resolve more photons than it has pixels (Fig. 2.3(b)).

Additionally, it should be mentioned that due to the meander structure of the nanowire (Fig. 2.1(a)), the SNSPD is polarization dependent. Light is more strongly absorbed when the electric field is polarized along the length of the nanowire [33, 39]. This can make a noticeable difference in detection events for photon counting experiments, especially for multi-pixel devices where each pixel is oriented in the same direction. Care must also be taken, when choosing the correct bias current I_{bias} (Fig. 2.2(a)). If the current is too high, the nanowire can enter a static resistive state, also called “latched” state, where the detector is insensitive to subsequent photons [39].

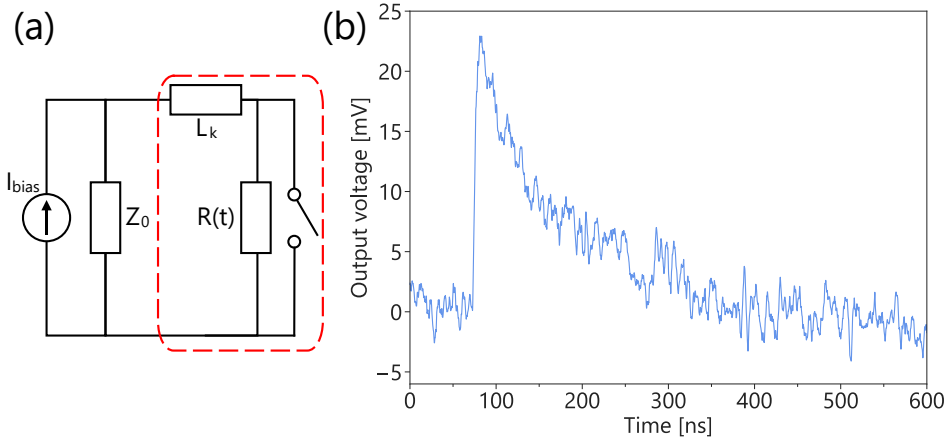


Figure 2.2: (a) Electrical circuit of an SNSPD (red dashed line outlines the nanowire meander). The absorption of a photon is represented by an opened switch, where the resistance of the wire $R(t)$ increases with hotspot formation. L_k is the kinetic inductance of the wire. The device is direct current biased at I_{bias} and an output signal is measured across the load impedance Z_0 (adapted from [6]). (b) Typical amplified electrical output pulse of an SNSPD measured with an oscilloscope.

2.1.3 Detector Characteristics

This section will give a brief overview of the characteristics of a (multi-pixel) superconducting nanowire single-photon detector that are important for this thesis.

Detection Efficiency

The first key characteristic of any detector is the detection efficiency η , which is the probability of detecting an output pulse as a result of an impinging photon. Generally the efficiency depends on the wavelength of the photons. Therefore, detector material and design are typically optimized to detect light in a given wavelength range. In any experiment photons can be lost before reaching the detector due to reflections, scattering or absorption, which will limit the efficiency to be below unity (100%). The overall system detection efficiency of the device η_{sde} can be split into three parts:

$$\eta_{sde} = \eta = \eta_{\text{coupling}} \cdot \eta_{\text{absorption}} \cdot \eta_{\text{registering}} \cdot \quad (2.1)$$

The first contribution describes how efficient the light can be coupled from the light source to the detector. The absorption efficiency depends on the detector material and geometry and the registering efficiency is the probability that an electrical signal is generated by the detector after the absorption of a photon [6]. The highest demonstrated efficiencies are 93% for WSi [7] and 98% for MoSi [56] SNSPDs.

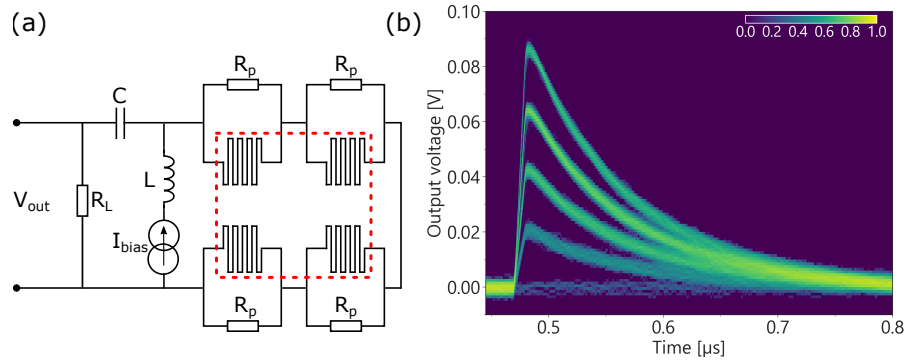


Figure 2.3: (a) Circuit diagram of the 4-pixel SNSPD (a 2×2 array) used in this thesis. The active area of the device is marked by the dashed red square. All detectors are wired in series, which enables a single-channel readout and are direct current biased from a current source I_{bias} (via a bias-tee of inductance L and capacitance C). The output voltage pulse V_{out} is measured across the load resistor R_L [27]. (b) Oscilloscope traces displaying the linear scaling of the five possible electrical response signals of the 4-pixel detector (used in this thesis) as a heat-map [27].

Dark Counts

Detection events caused by stray light or intrinsic electrical noise of the detector are considered to be false detection events. These uncorrelated events are called dark counts, as they also occur when no light is incident on the device [39]. To determine this figure of merit all input light gets blocked to the detector and a count rate gets measured for an extended period of time. SNSPDs are known for their unmatched low dark-count rates, typically below 200 counts per second. However, rates of 10^{-4} Hz have also been demonstrated [8].

Cross-Talk

In addition to dark noise, multi-pixel detectors can also exhibit conditional noise called cross-talk. A false detection event arising from a neighboring pixel firing. This effect depends on the bias current and the detector architecture, especially when the individual pixels are wired in series (Fig. 2.3(a)). If a pixel detects a photon it will generate an electrical output pulse, which will cause small current density fluctuations. In some cases these fluctuations, in combination with the bias current I_{bias} , can lead to the breakdown of the superconducting state of a neighboring pixel and thus a false detection event.

Important to reduce the effect of cross-talk is a bias plateau [18, 57], a saturated detection efficiency for a wide margin in operating bias currents. The plateau allows the detector to be operated further away from the critical current density J_c , diminishing the effect of cross-talk caused by current density fluctuations [18].

Measuring and modeling cross-talk is not trivial, but has been applied to multi-pixel photon counters based on avalanche photodiodes or silicon photomultipliers [46–53].

2.2 Quantum Detector Tomography

Measurements are essential for any type of quantum experiment, as they reveal the properties of the investigated process, material or phenomenon. It is desired to be able to fully describe an experiment. This means to describe the triad of state preparation, evolution and detection. Quantum state tomography will characterize unknown quantum states by performing measurements on an ensemble of identically prepared states, whereas, quantum process tomography will characterize the evolution of states based on precise knowledge of the initial and final quantum states. Both of these require well-characterized detectors, which makes quantum detector tomography the key feature of the description of quantum experiments [39].

Partial calibration of figures of merit or building elaborate models for detectors are alternative characterization methods. However, the model-based approach requires knowledge about the underlying physics and working principle of the detector, as well as detector parameters such as efficiency and noise. As quantum detectors become more and more complex, understanding and modeling them becomes increasingly difficult [41]. On the other hand, quantum detector tomography treats the device as a black-box with no prior knowledge required [40].

2.2.1 General Introduction

Quantum detector tomography yields a full quantum mechanical description of the detector under test. The characterization consists of reconstructing the positive operator valued measure (POVM) operators corresponding to the device. This can be achieved by measuring the detector response to a set of known input states $\{\rho\}$. Given these input states, the Born rule describes the probability of obtaining outcome n :

$$p_{\rho,n} = \text{Tr} [\rho \pi_n] , \quad (2.2)$$

where $\{\pi_n\}$ is the detector POVM [40]. In order to describe a physical measurement device, these operators need to be positive semi-definite, which ensures positive probabilities and they need to sum to one:

$$\pi_n \geq 0, \quad \sum_n \pi_n = \mathbb{1} . \quad (2.3)$$

Additionally, the set of input states $\{\rho\}$ must be tomographically complete. That means, the set must include all states the detector might be sensitive to. Mathematically that means the input states need to span the Hilbert space of the detector. The task behind detector tomography is to invert Eq. (2.2) subject to the aforementioned constraints [41].

2.2.2 POVM Formalism

In quantum mechanics, the quantum measurement postulate describes the effects of measurements on quantum systems. The postulate provides the probabilities of different outcomes occurring and also the post-measurement state of the system. However, for some applications e.g. photon counting experiments, where each state is only measured once, the post-measurement state of the system is of no interest. In these cases the so called POVM formalism can be used [58].

If a system is in the state $|\psi\rangle$ and a measurement described by the measurement operators M_n is performed upon the system, then the probability of outcome n is given by

$$p(n) = \langle \psi | M_n^\dagger M_n | \psi \rangle . \quad (2.4)$$

By defining $\pi_n \equiv M_n^\dagger M_n$, it follows from the quantum measurement postulate that π_n is a positive operator which also sums to one. Therefore, the set of operators π_n are sufficient to determine the probabilities of possible measurement outcomes. The complete set $\{\pi_n\}$ is known as a positive operator valued measure (POVM) [58].

2.2.3 Photon-Number Resolving Detectors

Photon-number resolving detectors are capable of partially resolving the incident number of photons, by assigning each of their multiple outcomes to an input photon number. However, such a detector rather measures the input photon-number statistics. This stems from a non-unity efficiency and noise, which does not allow for a one-to-one mapping. An intuitive option of expressing their POVM elements $\{\pi_n\}$ is the photon-number basis [39]

$$\pi_n = \sum_{m,j=0}^{\infty} \langle m | \theta^{(n)} | j \rangle | m \rangle \langle j | . \quad (2.5)$$

In the case of phase-insensitive detectors, which merely register the number of photons without phase information, the off-diagonal POVM elements can be assumed to be zero. Therefore, Eq. (2.5) simplifies to

$$\pi_n = \sum_{m=0}^{\infty} \theta_m^{(n)} | m \rangle \langle m | , \quad (2.6)$$

where $\theta_m^{(n)} = \theta_{m,m}^{(n)} = \langle m | \theta^{(n)} | m \rangle$ represents the diagonal elements [40] and can therefore be seen as the probability of receiving detection outcome n given m incident photons.

The choice of input states is important for quantum detector tomography measurements. Not only do the input states need to span the Hilbert space of the POVM set, they also need to be well characterized, available in large variety and quantity and experimentally

feasible [39]. Owing to the fact that the POVM elements are now represented in the photon-number basis (Eq. (2.6)), the Fock states $\{|n\rangle\}$ seem to be the first choice. However, higher order Fock states are by no means readily available, as they are difficult to produce [39]. When dealing with optical detectors, the set of coherent states $\{|\alpha\rangle\}$ turns out to be the perfect choice [40]. They are overcomplete and can be easily generated with lasers in large quantity. By attenuating a coherent state $|\alpha\rangle$ e.g. with variable optical attenuators by a factor of $1 - \eta$, the resulting state $|\eta\alpha\rangle$ is again a coherent state with lower mean photon number. Therefore, they are a suitable set to use for detector tomography. Additionally, coherent states can be easily expanded in the photon-number basis:

$$|\alpha\rangle = \sum_{i=0}^{\infty} e^{-\frac{|\alpha|^2}{2}} \frac{\alpha^i}{\sqrt{i!}} |i\rangle, \quad (2.7)$$

with photon number i and the amplitude of the coherent state $|\alpha|$ [59]. Equation 2.6 suggests that each POVM π_n contains an infinite amount of elements, which would not be possible to reconstruct. Fortunately, photon-number resolving detectors show a saturation in their outcome statistics. This means, there exists a maximum photon number the detector can resolve, or in other words, there exists a maximum photon number after which the detector will always respond with the same outcome. Consequently, the expansion of the POVM elements in Eq. (2.6) can be truncated at a sufficiently large photon number $M - 1$, where M is then the maximum Hilbert space dimension of the detector [39]

$$\pi_n = \sum_{m=0}^{M-1} \theta_m^{(n)} |m\rangle\langle m|. \quad (2.8)$$

A single coherent state, truncated at a photon number $M - 1$ in the photon number basis (Eq. (2.7)), would be enough to span the M -dimensional Hilbert space of the detector, as it is tomographically complete. However, it is not practical in an experiment, as it would require a disproportionate amount of time to gain sufficient statistics for all photon numbers. Instead, multiple coherent input states, spaced in a reasonable way, are used to enable appropriate measurement times [41].

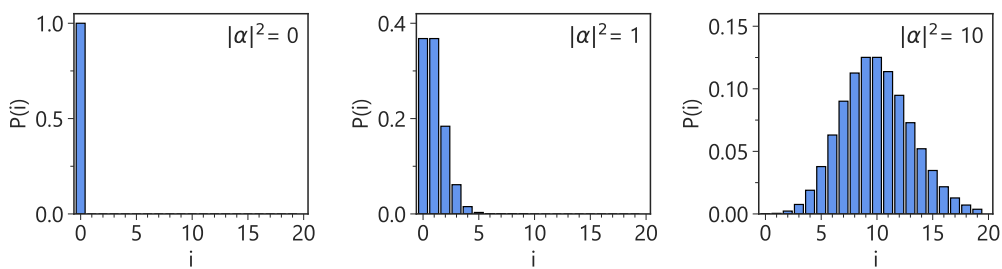


Figure 2.4: Poisson distributions for coherent states with mean photon numbers 0, 1, 10. The amplitude of the distributions decreases with increasing mean photon numbers $|\alpha|^2$.

As mentioned before in Section 2.2.1, the task behind detector tomography is to invert Eq. (2.2). In order to do that, the POVM elements of the detector π_n and the coherent input states, represented by their density matrices $\rho_d = |\alpha_d\rangle\langle\alpha_d|$ with $d \in [0, D-1]$ for a total of D coherent input states, will be expanded in the photon number basis according to Eq. (2.8) and Eq. (2.7) respectively. Using the relations for the trace

$$\text{Tr} [\hat{O}] = \sum_k \langle k | \hat{O} | k \rangle \quad (2.9)$$

and the Dirac delta function $\langle x | y \rangle = \delta_{x,y}$, the Eq. (2.2) describing the probabilities $p_{d,n}$ will transform as follows [39]

$$\begin{aligned} p_{d,n} &= p_{\rho_d,n} = \text{Tr} [\rho_d \pi_n] \\ &= \text{Tr} \left[\sum_{i=0}^{M-1} e^{-|\alpha_d|^2} \frac{\alpha_d^i \alpha_d^{*i}}{i!} |i\rangle\langle i| \sum_{m=0}^{M-1} \theta_m^{(n)} |m\rangle\langle m| \right] \\ &= \text{Tr} \left[\sum_{i=0}^{M-1} \sum_{m=0}^{M-1} e^{-|\alpha_d|^2} \frac{|\alpha_d|^{2i}}{i!} \theta_m^{(n)} |i\rangle\langle i|m\rangle\langle m| \right] \\ &= \sum_k \langle k | \sum_{i=0}^{M-1} e^{-|\alpha_d|^2} \frac{|\alpha_d|^{2i}}{i!} \theta_i^{(n)} |i\rangle\langle i| k \rangle \\ &= \sum_{i=0}^{M-1} e^{-|\alpha_d|^2} \frac{|\alpha_d|^{2i}}{i!} \theta_i^{(n)} \\ &= \sum_{i=0}^{M-1} F_{d,i} \Pi_{i,n}. \end{aligned} \quad (2.10)$$

The matrices are defined as $\Pi_{i,n} = \theta_i^{(n)}$ and

$$F_{d,i} = e^{-|\alpha_d|^2} \frac{|\alpha_d|^{2i}}{i!}, \quad (2.11)$$

where \mathbf{F} is a representation of the Poisson distribution of the coherent states with mean photon numbers $|\alpha_d|^2$ (Fig. 2.4). The equation is divided into two known parts: the matrix $\mathbf{F}_{D \times M}$ containing the known coherent probe states expanded in the photon number basis and truncated at a photon number $M-1$, to achieve a maximum Hilbert space dimension M , and the matrix $\mathbf{P}_{D \times N}$, with elements $P_{d,n} = p_{d,n}$ containing the measurement statistics of an N -outcome detector; and one unknown part: the matrix $\mathbf{\Pi}_{M \times N}$ containing the POVM set of the detector [40]. Finally, Eq. (2.10) can be recast as the matrix equation

$$\mathbf{P} = \mathbf{F} \mathbf{\Pi}. \quad (2.12)$$

A direct inversion of this matrix equation is prone to noise and may give unphysical results, which would not fulfill the constraints from Eq. (2.3). Therefore, an optimization technique is utilized to reconstruct the POVM set describing the detector [39].

2.2.4 Optimization

Optimization techniques try to find the solution which minimizes a specified “cost function” under given constraints [39]. In the case of Eq. (2.12), the unknown matrix $\mathbf{\Pi}$ has to be found, such that the difference in the matrices on the left-hand and right-hand side of the equal sign is minimized. A measure to evaluate the difference in matrices is given by the Frobenius norm $\|\mathbf{A}\|_2$, which is defined as follows [60]

$$\|\mathbf{A}\|_2 = \sqrt{\sum_i \sum_j |A_{i,j}|^2}. \quad (2.13)$$

Hence, a suitable cost function for reconstructing the POVM elements of the detector is given by

$$\|\mathbf{P} - \mathbf{F}\mathbf{\Pi}\|_2. \quad (2.14)$$

However, a reconstruction based on this cost function can lead to an irregular structure in the POVM elements [41], which manifests itself in sudden jumps between elements. Therefore, a convex quadratic filter function

$$g(\mathbf{\Pi}) = \gamma \sum_{i,n} \left(\theta_i^{(n)} - \theta_{i+1}^{(n)} \right)^2 \quad (2.15)$$

is introduced into the cost function, where the weight $\gamma \in [0, 1]$ is also called the smoothing parameter. The function $g(\mathbf{\Pi})$ will favor smooth POVM elements, which means the difference of neighboring elements is small. The smoothing is valid, since realistic quantum detectors have a finite efficiency η , which imposes a smoothness on the distribution of $\theta_i^{(n)}$ [40]. In fact, a non-smooth distribution would favor specific impinging photon numbers over their direct neighbors, which would not make physical sense for these kinds of lossy detectors. Finally, the convex optimization problem is given by:

$$\begin{aligned} \min \{ \|\mathbf{P} - \mathbf{F}\mathbf{\Pi}\|_2 + g(\mathbf{\Pi}) \} \\ \text{subject to } \pi_n \geq 0, \quad \sum_n \pi_n = \mathbf{1}, \end{aligned} \quad (2.16)$$

where the constraints introduced in Eq. (2.3) must also be fulfilled [40].

2.2.5 Theoretical POVMs

To visualize the distribution of the POVMs in the photon number basis, a model of a theoretical POVM will be utilized. This model starts with the POVM of a lossless and phase-insensitive detector $\mathbf{\Pi}_{\text{lossless}}^{\text{theo}}$ that can detect up to four photons, however, can not distinguish four from more than four photons:

	π_0	π_1	π_2	π_3	π_4
$ 0\rangle\langle 0 $	1	0	0	0	0
$ 1\rangle\langle 1 $	0	1	0	0	0
$ 2\rangle\langle 2 $	0	0	1	0	0
$ 3\rangle\langle 3 $	0	0	0	1	0
$ 4\rangle\langle 4 $	0	0	0	0	1
$ 5\rangle\langle 5 $	0	0	0	0	1
$ 6\rangle\langle 6 $	0	0	0	0	\vdots

To make this model more realistic, loss will be introduced via the loss matrix

$$L_{i',i} = \binom{i}{i'} \eta^{i'} (1-\eta)^{i-i'}, \quad (2.17)$$

which is a binomial distribution describing the probability of retaining i' out of i photons with a finite efficiency η of the detector [41]. By multiplying \mathbf{L} and $\mathbf{\Pi}_{\text{lossless}}^{\text{theo}}$ the POVM of a lossy detector $\mathbf{\Pi}_{\text{lossy}}^{\text{theo}}$ can be calculated. Plotting the columns of this matrix, which correspond to the five possible outcomes of the theoretical detector, against the photon numbers, reveals the expected smooth distribution for lossy detectors shown in Fig. 2.5.

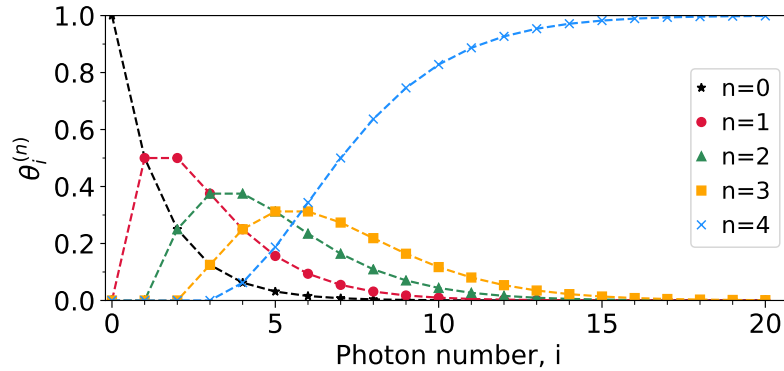


Figure 2.5: POVM elements of the modeled lossy and phase-insensitive detector with an efficiency of $\eta = 0.5$ in the photon number basis (here shown up to $|20\rangle\langle 20|$) for all five outcomes: no-click (black), one click (red), two clicks (green), three clicks (yellow), and at least four clicks (blue).

Equivalently, this smooth distribution can also be observed for a photon-number resolving time multiplexed detector capable of detecting up to eight photons and a binary avalanche photodiode [40, 41].

Reconstruction Performance

It is possible to assess the performance of the reconstruction procedure introduced in Section 2.2.4. To do that, the POVM of the lossy detector $\mathbf{\Pi}_{\text{lossy}}^{\text{theo}}$ is used to calculate a theoretical measurement statistics matrix \mathbf{P}^{theo} according to Eq. (2.12), with coherent input states $|\alpha|^2 \in [0, 50]$ in steps of one populating the coherent input state matrix \mathbf{F}^{theo} . Subsequently, these matrices are used to infer again the POVM of the modeled detector (now labeled $\mathbf{\Pi}^{\text{rec}}$) by following the optimization problem in Eq. (2.16). The performance is evaluated by calculating the fidelity

$$\mathcal{F}(n) = \text{Tr} \left[\sqrt{\sqrt{\pi_n^{\text{theo}}} \pi_n^{\text{rec}} \sqrt{\pi_n^{\text{theo}}}} \right]^2, \quad (2.18)$$

where the POVM elements are normalized according to $\pi_n / \sum_n \pi_n$ to ensure $\mathcal{F} \in [0, 1]$ [41]. The fidelity calculates to $\mathcal{F} \geq 99.8\%$ for all outcomes n , which indicates an excellent performance of the optimization procedure.

POVM Purity

Additionally, to assess the POVMs of the different detector outcomes π_n , it is possible to define a purity for each detection outcome n as [53, 61]

$$\text{Purity}(\pi_n) = \frac{\text{Tr}[(\pi_n)^2]}{(\text{Tr}[\pi_n])^2}. \quad (2.19)$$

This measure is in full analogy to the purity of quantum states and satisfies the boundaries given by

$$\frac{1}{M} \leq \text{Purity}(\pi_n) \leq 1. \quad (2.20)$$

For a perfect detector, where n photons and only n photons will lead to an n -click event, the purity equals unity. The lower bound is determined by the Hilbert space dimension M . Therefore, the purity can also be seen as the photon-number resolving performance of the detector, as the physical meaning of a non-pure (non-unity) purity of π_n is that multiple orthogonal input states (in the photon number basis) can lead to the same detection outcome n . Hence, an effective Hilbert space dimension can be defined as

$$M_{\text{eff}}(n) = \frac{1}{\text{Purity}(\pi_n)}, \quad (2.21)$$

which is an estimation of how many orthogonal input states contribute to outcome n with significant probabilities [53, 61].

2.2.6 Detector Wigner Functions

Quasi-probability distributions, such as the Wigner function, enable the visualization of the detection outcomes of the detector in phase space. It is possible to plot a Wigner function for all reconstructed POVM elements π_n , which is given by

$$W^{(n)}(x, p) = \frac{1}{\pi\hbar} \int_{-\infty}^{\infty} dy \langle x - y | \pi_n | x + y \rangle e^{\frac{2ip y}{\hbar}}, \quad (2.22)$$

where $(x, p) \in \mathbb{R}^2$ are phase space coordinates of a single-mode with $\alpha \in \mathbb{C}$. For phase-insensitive detectors, the Wigner functions will have rotational symmetry around the origin [41]. Features, such as negativity in the Wigner function that indicates non-classicality, will also be revealed by the detector Wigner functions, which will classify the detectors as quantum detectors with the ability to detect non-classical optical states [39].

To be able to perform quantum detector tomography, the detector response has to be measured for a set of known input states. As introduced in Section 2.2.3, coherent states are ideal candidates. Coherent states are completely characterized by their mean photon number $|\alpha|^2$, this means the states used for the experiment have to be calibrated, to determine their mean photon numbers. The calibration process will be described in this chapter.

3.1 Experimental Setup

The experimental setup to calibrate the input states is shown in Fig. 3.1. The coherent input states are generated by a 1556 nm pulsed laser (*ALPHALAS PICOPOWER-LD-1550-50-FC*). A “pulse power position setting” of 3.5 is used in combination with a repetition rate of 500 kHz. This ensures undistorted laser pulses with a pulse length of 9 ps. To reach the single-photon level, two computer controlled variable optical attenuators are used to vary the pulse energy of the pulses. As explained in Section 2.1.2, superconducting nanowire single-photon detectors (SNSPDs) are polarization dependent. Therefore, the polarization of the photons can be adjusted (to maximize the count rate) via manual fiber polarization controllers, which utilize stress-induced birefringence produced by a single mode fiber wrapped around three spools. Finally, the input states are detected by a calibrated 1-pixel SNSPD with an efficiency $\eta_{\text{cal}} = (83 \pm 5) \%$, located in a helium sorption fridge at 0.8 K (both from *Photon Spot, Inc.*). The detector is direct current biased at $9.2 \mu\text{A}$ for optimal operation. To minimize the effects of noise, the output pulses from the 1-pixel SNSPD are measured in a coincidence window of 15 ns synchronized to the laser pulses, using a time tagger (*Swabian Instruments Time Tagger Ultra*). A time tagger counts the number of times a specified voltage threshold is exceeded (or deceeded). For this detector a threshold of 50 mV is used, which was determined using an oscilloscope. To avoid triggering on noise on the falling edge of the output pulse (see Fig. 2.2(b) for reference) an artificial dead time that has to be larger than the coincidence window is set in the time tagger. A dead time of 60 ns is used, meaning that after a measured signal no further events will be counted for this duration.

A total of 101 coherent states, for attenuations $\alpha \in [30, 80]$ in steps of 0.5 dB, are measured across the entire sensitive regime of the 1-pixel SNSPD. This corresponds to outcomes, where the detector will always respond with a click for all incoming laser pulses (30 dB) or will almost never click (80 dB). For each coherent state the click statistics were obtained for 5×10^5 pulses or equivalently one second. Note, that the most reliable method to set the

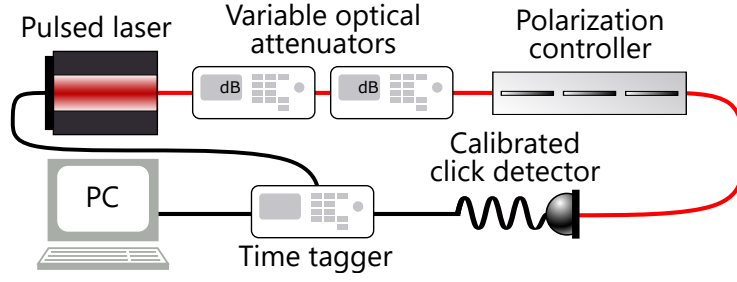


Figure 3.1: Experimental setup for the input state calibration. A 1556 nm pulsed laser generates coherent states at a repetition rate of 500 kHz. The states can be attenuated using two variable optical attenuators before they are detected by the calibration detector (1-pixel SNSPD), which is located in a cryostat at 0.8 K. The output pulses from the detector are measured in synchronization with the laser pulses using a computer controlled time tagger. The red line represents an optical fiber and the black line a coaxial cable.

attenuation of the attenuators is to initialize them by setting both devices to no attenuation (0 dB) and then directly to the attenuation of choice. Both devices are always adjusted symmetrically (set to $\frac{\alpha}{2}$ to achieve a total attenuation of α) and all measurements are carried out from low to high attenuations, to avoid hysteresis and nonlinearities of the devices.

3.2 Analysis

To calibrate the coherent input states, the mean photon numbers corresponding to different attenuation settings in the experiment need to be determined. A laser is a source of coherent states, whose photon number distributions follow Poissonian statistics [62]

$$P(i) = \frac{(\eta_{\text{cal}}\bar{n})^i}{i!} e^{-\eta_{\text{cal}}\bar{n}}, \quad (3.1)$$

describing the probability of having i photons in a coherent state with a mean photon number of $|\alpha|^2 = \bar{n}$ and efficiency η_{cal} of the calibration detector. This also applies to the laser used for this thesis, as it showed a second-order correlation function of $g^{(2)}(0) = 1.00002(34)$ across the investigated power range (for further details see Section 3.3), where $g^{(2)}(0) = 1$ for perfectly coherent light [62].

For click-detectors, the quotient of the count rate (measured clicks per second) and the repetition rate of the pulsed laser can intuitively be seen as the probability of receiving a click. The click probability can also be represented using the probability of not receiving a click, which is given by $P(0)$, the probability of not having a photon in the coherent state. Ultimately it follows:

$$p_{\text{click}} = \frac{\text{count rate}}{\text{rep. rate}} = 1 - p_{\text{no click}} = 1 - P(0) = 1 - e^{-\eta_{\text{cal}}\bar{n}}. \quad (3.2)$$

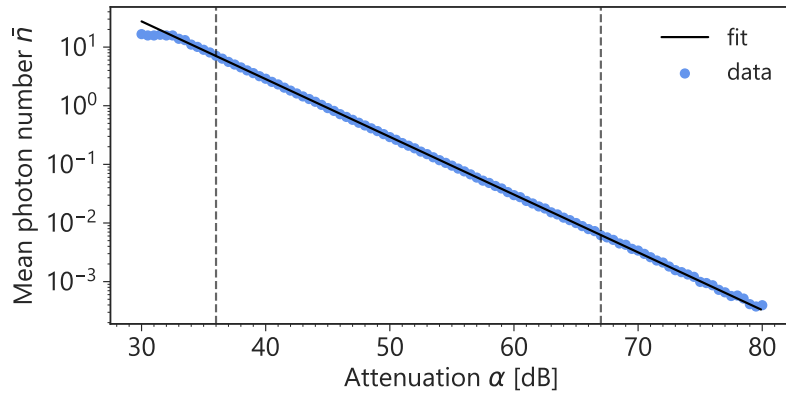


Figure 3.2: Mean photon number \bar{n} on a logarithmic scale vs. attenuation α in dB. The linear fit (black line) is based on measurement data within the marked region (vertical dashed lines).

By rearranging Eq. (3.2) it is possible to find the mean photon number per pulse as

$$\bar{n} = -\ln\left(1 - \frac{\text{count rate}}{\text{rep. rate}}\right) \frac{1}{\eta_{\text{cal}}}, \quad (3.3)$$

which depends on measurement data and the efficiency of the calibration detector. Using Eq. (3.3) the mean photon number per pulse is calculated for all coherent input states and plotted (on a logarithmic scale) against the corresponding attenuation α (Fig. 3.2). This allows for a linear fit, which is used to calculate the mean photon number for any attenuation setting via the expression:

$$\bar{n} = 10^{b+m\cdot\alpha}, \quad (3.4)$$

where $b = 4.393_{-0.025}^{+0.027}$ is the y-axis intercept, $m = -0.09848 \pm 0.00008$ is the slope of the linear fit and α is the attenuation in decibel. The larger error for the y-axis intercept b stems from the uncertainty in the efficiency of the calibration detector of $(83 \pm 5)\%$. The upper and lower bounds are calculated by repeating the previous analysis with $83\% - 5\% = 78\%$ and $83\% + 5\% = 88\%$ efficiency η_{cal} of the calibration detector, respectively. Note, that the slope m of the fit stays the same between all three fits (for the original data and the upper and lower error bounds), as the 5% error on the efficiency of the calibration detector acts as a constant offset on the resulting mean photon number per pulse.

Fit Boundaries

The linear fit to determine the mean photon number per pulse (Fig. 3.2) is only based on measurement data within the region marked by the vertical dashed lines. The lower boundary stems from a saturation effect of the 1-pixel SNSPD, which occurs when too

many photons are incident. Above a certain mean photon number the detector will click for every laser pulse, which means the click probability $p_{\text{click}} = 1$. Therefore, the dependency of the mean photon number to attenuation is no longer accurate, as the natural logarithm of zero is not defined (compare Eq. (3.3)).

The upper boundary is set due to a chosen limit to the Poisson error on the counting statistics. The maximum relative error on the counts was chosen to be 5%, in order to be negligible in comparison to the uncertainty in the efficiency of the calibration detector. With this, it is possible to calculate the minimum number of counts needed to not exceed this chosen limit:

$$\frac{\sqrt{x}}{x} = \frac{1}{\sqrt{x}} \leq 5\% \Rightarrow x \geq 400, \quad (3.5)$$

where x is the number of counts and the fraction describes the relative Poisson error. That means, all measurement points to the right of the vertical dashed line in Fig. 3.2 are excluded from the fit, since they do not have sufficient statistics (not enough clicks were measured for these coherent input states).

Now that it is possible, to calculate the mean photon number per pulse only depending on the attenuation setting of the attenuators, the coherent input states have been calibrated. In the next section, the main quantum detector tomography measurement of the 4-pixel SNSPD will be described. Note, the input state calibration and the analysis were specifically described for the 4-pixel SNSPD detector tomography experiment. However, this is a general concept, which will be applied prior to any other measurement. An input state calibration is necessary before any measurement, as it is not guaranteed that the laser source is perfectly stable if it has been switched off in the meantime, which leads to slight variations in the coherent states. The only parameters that will change between measurements are the y -axis intercept b and the slope m of the linear fit, which determine the dependency of the mean photon numbers \bar{n} on the attenuations α in the experiment in Eq. (3.4).

3.3 Second-Order Correlation Function

The second-order correlation function $g^{(2)}$ can be used to determine the photon statistics of a light source. For quantum detector tomography it is important to know whether the generated input states are truly coherent, as the input state matrix \mathbf{F} in Eq. (2.11) assumes Poissonian statistics.

Typically, a Hanbury Brown-Twiss (HBT) experiment is carried out to assess the photon statistics of a light source. In an HBT experiment photons pass through a 50:50 beam splitter and are detected by a single-photon detector in either arm. A counter/timer will record the time τ that elapses between the start pulse from detector one and the stop pulse from detector two, while simultaneously counting the number of pulses from each detector [62]. It is apparent that for antibunched light (with sub-Poissonian photon statistics), where for

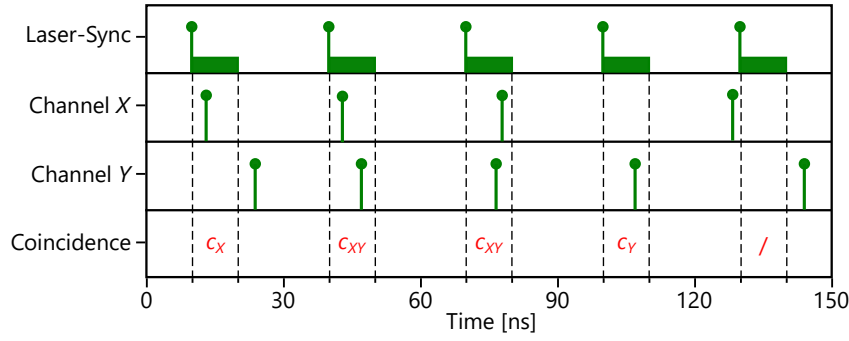


Figure 3.3: Schematic visualization of the coincidence counting for two channels/detectors. Only pulses within the 10 ns coincidence window after the laser-synchronization pulse are recorded. c_X and c_Y indicate a normal count from the detectors, whereas c_{XY} labels a coincidence count between the two detectors, which also entails both a count for c_X and c_Y (adapted from [63]).

example single photons with a long time interval between them are incident on the beam splitter, the counter/time will never record an event for $\tau = 0$, as the single photons are either detected by the first or the second detector and no coincidence counts can occur. The opposite of this occurs for bunched light (with super-Poissonian photon statistics), where always bunches of photons are incident at the 50:50 beam splitter, which will be distributed evenly into both arms. Hence, the probability of detecting a coincidence count for $\tau = 0$ is high.

For perfectly coherent light (with Poissonian photon statistics), which has random time intervals between photons, the probability of detecting a stop pulse is the same for any time interval τ and the second-order correlation function $g^{(2)}(\tau) = 1$. This enables a classification of the photon statistics of a light source by comparing the second-order correlation function for the time interval of $\tau = 0$ [62]:

$$g^{(2)}(\tau = 0) \begin{cases} > 1 & , \text{super-Poissonian} \\ = 1 & , \text{Poissonian} \\ < 1 & , \text{sub-Poissonian} . \end{cases} \quad (3.6)$$

To classify the photon statistics of the laser used in this thesis, a slightly different approach is used. In Chapter 5 a 4-bin spatially multiplexed detector is build to perform detector tomography. However, the experimental setup consisting of three 50:50 beam splitters that split incoming laser pulses into four detection channels enables a direct calculation of the second-order correlation function $g^{(2)}$ of the light source. A time tagger records detection events in a 10 ns coincidence window, synchronized to the laser pulses, from all individual detectors as well as coincidences between any two of the detectors (see Fig. 3.3 as reference). As only two detectors are necessary for a $g^{(2)}$ -measurement, this setup of four detectors enables a total of six measurements, which ultimately increases the accuracy of the resulting $g^{(2)}(0)$ -value for the photon statistics of the laser. The measurement is

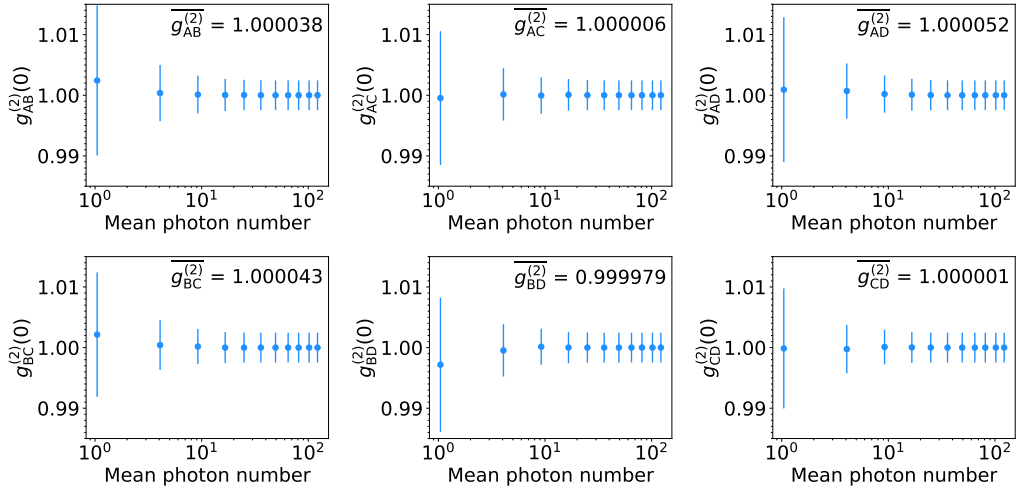


Figure 3.4: Second-order correlation function $g^{(2)}(0)$ as a function of the mean photon number for all six combinations of two of the four detectors A, B, C and D. The weighted mean calculated from values for different mean photon numbers is displayed for each combination.

performed across the entire power range of the detectors, which includes mean photon numbers $|\alpha_d|^2 \approx d^2$ for $d \in [0, 11]$.

The second-order correlation function for a time interval of $\tau = 0$ and for detectors X and Y can be calculated using the formula [64]:

$$g_{XY}^{(2)}(0) = \frac{c_{XY}c_0}{c_X c_Y}, \quad (3.7)$$

where c_{XY} is the coincidence count rate between detector X and Y , c_X and c_Y are the count rates of detector X and Y respectively and c_0 is the repetition rate of the laser. This calculation is carried out for all mean photon numbers $|\alpha_d|^2$ and for any combination of two of the four detectors A, B, C and D. The error $\Delta g_{XY}^{(2)}(0)$ of this measurement is calculated using Gaussian error propagation based on assuming Poisson errors on the counting statistics $\Delta c = \sqrt{c}$, whereas the standard deviation between the recorded repetition rates is used as the uncertainty on c_0 , as the repetition rate is very stable.

In Fig. 3.4 the second-order correlation function at $\tau = 0$ is plotted for all combinations against the mean photon number of the coherent input states. Afterwards, a weighted mean for the $g^{(2)}$ -values for different mean photon numbers is calculated for each of the six combination of two detectors (see Appendix A for calculations). Finally, the mean of the weighted means is calculated in order to obtain a value of $g^{(2)}(0) = 1.00002(34)$ that characterizes the photon statistics of the laser source as Poissonian. Hence, the light pulses of the laser can be safely assumed to be coherent. The uncertainty is calculated using Gaussian error propagation based on the standard error of the weighted mean.

Detector Tomography:

4-Pixel Detector

4

This chapter describes the quantum detector tomography experiment of the 4-pixel SNSPD. First the experimental setup will be introduced as well as further important considerations such as the choice of coherent input states. Afterwards, the experimental data will be analyzed and prepared for the tomographic reconstruction of the POVM matrix Π that characterizes the device. Lastly, the POVM elements will be used to define the main figures of merit: efficiency, dark-count probability and cross-talk probability and to visualize the detector outcomes in phase space using the Wigner function representation. The chapter ends with a reliability test of the POVMs, when decreasing the number of coherent input states and thus the Hilbert space dimension. These considerations are important for increasing detector array sizes, as the necessary time for the reconstruction and the computational demand will also increase. Parts of this chapter have been submitted for publication [65].

4.1 Experimental Setup

Before conducting a measurement, it is important to determine the optimal bias current I_{bias} for the 4-pixel SNSPD. As mentioned in the end of Section 2.1.2, the detector needs to be operated close to, but beneath the critical current to avoid latching but achieve maximum efficiency. Therefore, a bias curve will be recorded, where the count rate for a fixed coherent input state will be measured with a time tagger while varying the bias current. The 4-pixel device has five possible outcomes corresponding to different voltage thresholds (see oscilloscope traces in Fig. 4.1(a) for reference). For this measurement, the lowest voltage threshold for the “at least 1-click” event will be used. Hence, all click events will be registered, as the time tagger counts the number of times the chosen voltage threshold is exceeded. A clear bias plateau shown in Fig. A.1, reveals a region of possible bias currents I_{bias} .

Additionally, the optimal voltage thresholds to read out the different outcomes of the 4-pixel device need to be found. Typically, an oscilloscope is utilized to manually find the different threshold levels. However, here an alternative method is used, which could be called a “threshold sweep”. For this, the 4-pixel SNSPD will detect a coherent state with a large enough mean photon number to allow for “at least 4-click” events, while the time tagger measures the count rate for varying voltage thresholds. By plotting the measured count rate on a logarithmic scale against the threshold, four steps can be seen, which correspond to the different outcomes of the detector (Fig. 4.1(b)). Note, that the

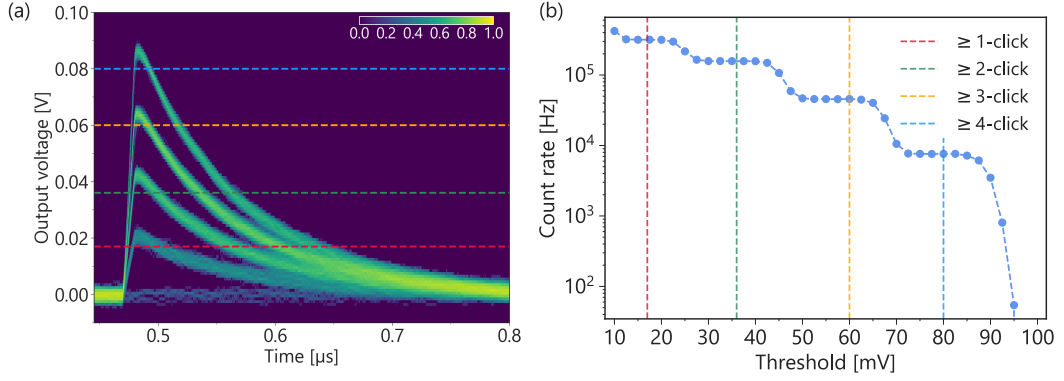


Figure 4.1: (a) Oscilloscope traces of the five possible electrical response signals of the 4-pixel detector as a heat-map (from [27]). The voltage thresholds according to the different outcomes determined in (b) are marked by the colored dashed lines. (b) Threshold sweep to determine the optimal voltage thresholds to read out the different outcomes of the 4-pixel device (for $I_{\text{bias}} = 17 \mu\text{A}$). The count rate is plotted on a logarithmic scale against the threshold. The steps reveal the possible threshold regimes for different outcomes. The chosen thresholds (colored vertical dashed lines, labeled in the legend) are 17 mV (≥ 1 -click), 36 mV (≥ 2 -click), 60 mV (≥ 3 -click) and 80 mV (≥ 4 -click).

steps depend on the choice of the bias current. Therefore, the measurement was carried out for multiple bias currents in the bias plateau. The steps were most pronounced for a bias current of $I_{\text{bias}} = 17 \mu\text{A}$, which will be the choice of the bias current for all subsequent measurements. More pronounced steps lead to a better differentiation of the different click events, which leads to more accurate results.

This threshold sweep is an intuitive way of determining the optimal thresholds. Starting at low thresholds, all click events will be counted by the time tagger, hence, the count rate will be high. After exceeding the maximum voltage pulse amplitude of the “at least 1-click” event (see Fig. 4.1(a) for reference), the time tagger will not count these events, which lowers the count rate. The same applies for the higher outcomes, until finally (above 95 mV) the maximum amplitude of the “at least 4-click” event has been exceeded and no counts will be measured. For thresholds under 10 mV the time tagger will trigger on the noise floor, which explains the increasing trend of the data points (Fig. 4.1(b)). Finally, the optimal thresholds located approximately in the middle of each step are 17 mV (≥ 1 -click), 36 mV (≥ 2 -click), 60 mV (≥ 3 -click) and 80 mV (≥ 4 -click).

For the quantum detector tomography experiment only one part will be changed, compared to the experimental setup of the input state calibration. The calibrated click detector will be substituted by the 4-pixel SNSPD (Fig. 4.2). This means, the pulsed laser will generate coherent states with a repetition rate of 500 kHz, which can afterwards be attenuated. The polarization of the photons will be adjusted, until the count rate is maximized. Subsequently, the coherent states will be detected by the 4-pixel SNSPD, which is located in a cryostat at 0.8 K and current biased at 17 μA . In an ensemble measurement, a time tagger synchronized to the laser pulses will count the different outcomes in a coincidence window of 15 ns, by

sequentially cycling through the previously determined thresholds. Additionally, a 150 ns artificial dead time is set in the time tagger, to avoid triggering on noise on the falling edge of the output signal, which could lead to false detection events.

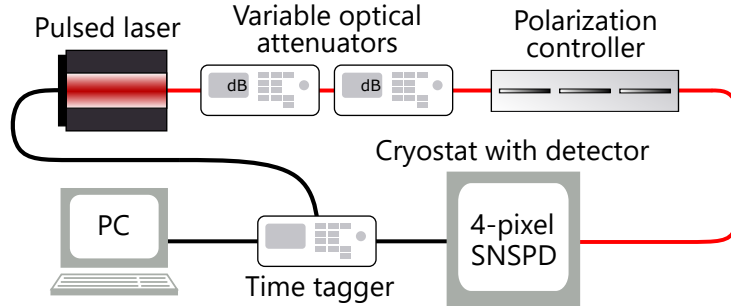


Figure 4.2: Experimental setup of the quantum detector tomography measurement of the 4-pixel SNSPD, which is located in a cryostat at 0.8 K. Just like the input state calibration measurement, a 1556 nm pulsed laser generates coherent states at 500 kHz, which can be attenuated before being detected by the 4-pixel SNSPD. A time tagger synchronized with the laser pulses will measure the outcome statistics of the 4-pixel device.

Choosing Input States

As mentioned in Section 2.2.3 the choice of coherent input states is important, to be able to span the Hilbert space of the detector and gain sufficient statistics, while maintaining appropriate measurement times. The 4-pixel SNSPD will saturate for pulses with a mean photon number above 300, which means that the detector will only respond with the highest outcome (an “at least 4-click” event). As a result, the largest coherent input state should have meaningful photon number contributions in the same regime. By choosing the amplitude of the coherent input states to scale quadratically, every photon number contributes roughly equally to the overall photon number statistics. This can be seen in Fig. 4.3, where the quadratically increasing coherent input states are plotted in blue and the resulting sum of the distributions (black dashed line) is smooth and remains approximately at the same amplitude for higher photon numbers. Additionally and very importantly, the 0-photon coherent input state needs to be measured. This can be done by blocking all input light to the detector, which results in only measuring dark counts originating from noise (see Section 2.1.3). Ultimately, this means the amplitude of the coherent input states will scale approximately quadratically $|\alpha_d|^2 \approx d^2$ with $d \in [0, 18]$, resulting in photon number distributions from 0 to 332 photons per pulse, which span the entire Hilbert space of the detector.

The coherent input states for $d \in [1, 18]$ are measured for 10 s for each threshold setting, to achieve sufficient statistics. However, the 0-photon coherent input state, which is essentially a dark count measurement, needs to be measured for a much longer time. This is because

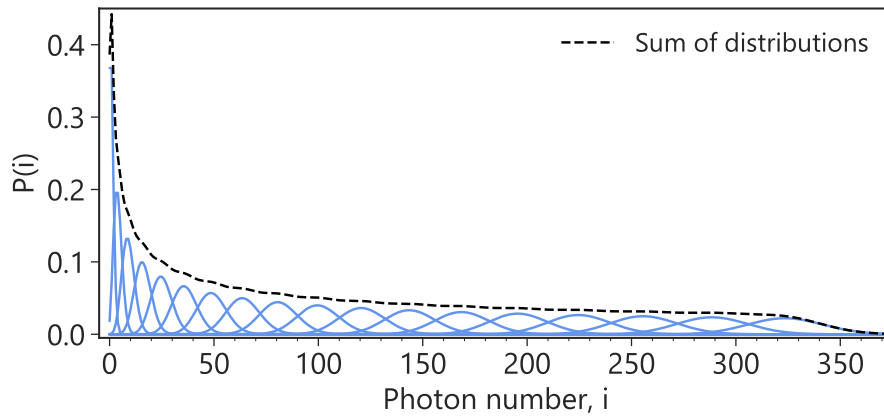


Figure 4.3: Photon number distributions from coherent states with quadratically increasing mean photon numbers from 1 to 324 (blue). The sum of the distributions (black dashed line) shows that each photon number contributes roughly equally, indicated by the smooth trend for higher photon numbers.

the 4-pixel SNSPD has a dark-count rate of approximately 200 dark counts per second. Since the measurement is set up to only count coincidences in a small window around the laser synchronization pulse, this results in a very small fraction of a second in which the dark counts will be counted. In fact, multiplying the coincidence window, the repetition rate of the laser and the expected dark-count rate leads to merely 3 expected dark counts per gated second. Note, that for this calculation the coincidence window is twice as large as the window set in the time tagger. This is because dark counts are uncorrelated with respect to the laser synchronization pulse. Therefore, any counts that occur up to 15 ns before and after the pulse are counted, leading to a window of 30 ns. At least 400 counts are needed to be below a 5% relative Poisson error on the counts (compare Eq. (3.5)), therefore, as only 3 dark counts are expected in a gated second, the 0-photon coherent input state needs to be measured for at least 134 s and will be measured for 600 s to achieve sufficient statistics. Note, that due to sufficient measurement statistics, the uncertainty on the registered counts is negligible in comparison with the uncertainty of the calibration process (efficiency of the calibration detector).

4.2 Analysis

The next step to perform detector tomography and reconstruct the POVM elements of the 4-pixel SNSPD is to construct the coherent input state matrix \mathbf{F} and the measurement statistics matrix \mathbf{P} . These matrices are constructed based on the Poisson distributions of the different mean photon numbers used in the experiment and the measurement outcomes of the 4-pixel SNSPD, respectively.

4.2.1 Coherent Input State Matrix

A total of $D = 19$ coherent input states were used in the experiment. The different mean photon numbers are calculated with Eq. (3.4) for the used attenuations, both can be found in Table A.1. These states are represented by the matrix $\mathbf{F}_{D \times M}$ (already introduced in Eq. (2.11)) with the entries following the Poisson distribution

$$P(i)|_d = F_{d,i} = e^{-|\alpha_d|^2} \frac{|\alpha_d|^{2i}}{i!}, \quad (4.1)$$

with $d \in [0, 18]$ and $i \in [0, 442]$. Each row of the matrix contains one of the $D = 19$ coherent input states, which is expanded in the photon number basis. For the following numerical calculations, it is necessary to truncate the coherent states, as it is not possible to process infinite contributions to the coherent state (compare Eq. (2.7)). The expansion is truncated at the maximum Hilbert space dimension M , which is chosen to include probability amplitudes at six standard deviations greater than the largest coherent input state

$$M = |\alpha_{d_{\max}=18}|^2 + 6 \cdot \sqrt{|\alpha_{d_{\max}=18}|^2} = 332 + 6 \cdot \sqrt{332} = 442. \quad (4.2)$$

The cutoff is chosen at six standard deviations to include all contributions greater than a threshold of 10^{-8} . This ensures that all meaningful contributions are included in the input state matrix \mathbf{F} . For a comparison of probability amplitudes at different standard deviations σ and the Poisson distribution of the largest coherent input state see Fig. 4.4.

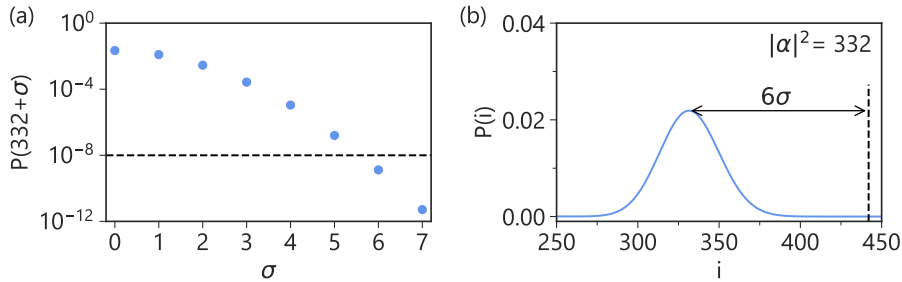


Figure 4.4: (a) Probability amplitudes of the largest coherent input state $P(332 + \sigma)|_{18}$ for standard deviations $\sigma \in [0, 7]$ on a logarithmic scale. The threshold of 10^{-8} is marked by the horizontal dashed line. (b) Poisson distribution of the coherent state with mean photon numbers of $|\alpha|^2 = 332$. The corresponding truncation limit of six standard deviations (6σ) is marked by the vertical dashed line.

Choosing an adequate truncation value for the coherent state expansion is crucial, as the reconstruction assumes coherent states in the input state matrix \mathbf{F} (compare Section 2.2.3). If the truncation is set to low, higher states are not represented correctly, which leads to a mixture of Poissonian and non-Poissonian states in the matrix \mathbf{F} and consequently an unreliable reconstruction of the POVM matrix $\mathbf{\Pi}$.

4.2.2 Measurement Statistics Matrix

As mentioned in Sections 2.1.2 and 4.1, the 4-pixel SNSPD has $N = 5$ possible outcomes, which enable the quasi-photon-number resolution, by placing a lower bound on the number of photons incident on the device. Experimentally, these outcomes are measured as “at least n -click” count rates c_n , with $n \in [0, 4]$, which correspond to at least n pixels firing. To simplify the notation, c_0 (at least 0 clicks) will correspond to the repetition rate of the laser (500 kHz). Due to small variations in the measurement time for different ensemble measurements, on a time scale of 500 kHz^{-1} , it can occur that count rates c_n are smaller by a few counts than count rates $c_{n' > n}$. Although, given the readout method of the time tagger, where the events $c_{n'}$ are contained in the events $c_{n < n'}$, this should not be possible. As an example, the “at least 3- and 4-click” events will also be counted for the threshold setting of the “at least 2-click” events, hence the term “at least” is used. Therefore, these cases are adjusted following the general rule:

$$\text{if } c_n < c_{n+1} : c_n = c_{n+1}. \quad (4.3)$$

Additionally, all count rates are corrected by subtracting the dark-count rate (from the measurement of the 0-photon coherent input state $|\alpha_0|^2$).

At this point, the outcomes c_n are not orthogonal, since the events $c_{n'}$ are contained in the events $c_{n < n'}$. To achieve orthogonal outcomes, the count rates are transformed using the expression

$$c'_n = \begin{cases} c_n, & \text{if } n = 4 \\ c_n - c_{n+1}, & \text{if } n \leq 3 \\ c_n - \sum_{n'=1}^4 c'_{n'}, & \text{if } n = 0, \end{cases} \quad (4.4)$$

such that c'_n now describes the “exactly n -click” count rates. The count rate for “at least 4-clicks” will not be transformed, since the detector has only four pixels, which makes it impossible for the device to distinguish four photons from more than four photons. The no-click or 0-click event is calculated by subtracting the sum of all other count rates from the repetition rate of the laser c_0 . This is possible, since all laser pulses that did not lead to any click event are considered to be a no-click event.

The last step to construct the measurement statistics matrix \mathbf{P} is to divide the transformed count rates by the repetition rate of the laser c_0 to calculate click probabilities. Thus, the matrix elements are given by

$$P_{d,n} = \frac{c'_n}{c_0} \Big|_d. \quad (4.5)$$

4.2.3 POVM Reconstruction

To reconstruct the positive operator valued measure (POVM) operators of the 4-pixel SNSPD, Eq. (2.16) is programmed into *Python* using the *CVXPY* module [66, 67]. The code is based on a *MATLAB* version from Alvaro Feito and can be found in Appendix A.

Based on the sizes of the previously constructed matrices $\mathbf{F}_{D \times M}$ and $\mathbf{P}_{D \times N}$, the POVM matrix $\mathbf{\Pi}_{M \times N}$ will be setup as a variable from the *CVXPY* module. All matrix elements are set to be non-negative and each row of the matrix should sum to one, which are the constraints of the optimization problem set in Eq. (2.16). Afterwards, the convex quadratic filter function (also called smoothing function) $g(\mathbf{\Pi})$ will be calculated according to Eq. (2.15). For this reconstruction a smoothing parameter of $\gamma = 0.1$ is used. Previous work has shown that the choice of the smoothing parameter does not affect the reconstructed POVM elements [41]. However, during the analysis in this work, this was found to be incorrect (at least specifically for SNSPDs). The choice of different smoothing parameters and their effect on the POVM elements will be discussed in more detail in Section 4.3.3. The optimization begins with an initial guess for the matrix elements of $\mathbf{\Pi}$. Subsequently, each iteration will follow the minimization given in Eq. (2.16), until the cost function is minimized.

4.3 Results

As mentioned in Chapter 1, the positive operator valued measures (POVMs) of a detector reveal many detector characteristics, such as efficiency, dark-count probability and cross-talk probability. This section will present the extracted figures of merit of the 4-pixel SNSPD, as well as detector Wigner functions and further results.

4.3.1 Reconstructed POVM Elements

A successful optimization of the problem from Eq. (2.16) based the experimental data for the 4-pixel SNSPD leads to the reconstructed POVM elements shown in Fig. 4.5 up to a photon number of $i = 50$. All five outcomes follow the expected smooth distribution in the photon number basis for lossy detectors shown in Fig. 2.5 for a modeled detector and show an overall close resemblance. The error bars stem from two additional POVM reconstructions (acting as lower and upper bounds) based on assuming an uncertainty in the amplitudes of the coherent input states, therefore on the coherent input state matrix \mathbf{F} , due to the uncertainty on the efficiency of the calibration detector of $\eta_{\text{cal}} = (83 \pm 5) \%$ (compare Section 3.2). The saturation of the $n = 4$ event means that the 4-pixel SNSPD will always respond with the largest outcome (an “at least 4-click” event) for input states with photon numbers $i > 45$.

To assess the reconstructed POVM elements of the 4-pixel SNSPD, the Purity (π_n) and the effective Hilbert space dimension $M_{\text{eff}}(n)$ are calculated for all five outcomes with

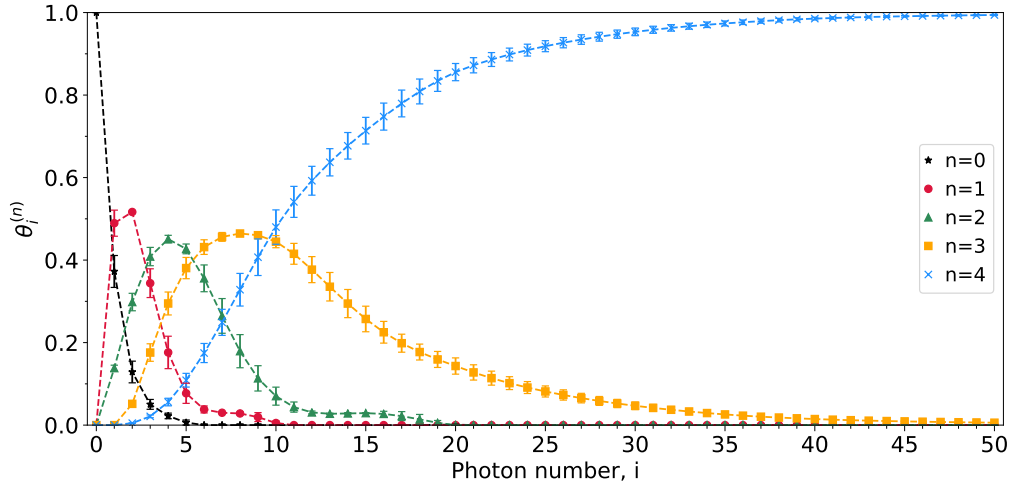


Figure 4.5: Diagonal elements of the reconstructed POVM operators π_n of the 4-pixel SNSPD in the photon number basis (here shown up to $|50\rangle\langle 50|$) for all $N = 5$ outcomes: no-click (black), one click (red), two clicks (green), three clicks (yellow), and at least four clicks (blue). Error bars are based on assuming 5% uncertainty on the efficiency of the calibration detector.

Eq. (2.19) and Eq. (2.21), respectively (see Table 4.1 for results). Overall, the purity or photon-number resolving performance of the 4-pixel device is not very good, as indicated by $\text{Purity}(\pi_n) \ll 1$. However, lossy detectors can not achieve a purity equal to unity, as photons from the input states will be lost or not detected and thus contribute to lower click events. Especially for this 4-pixel SNSPD, a 2×2 array of click-detectors, it is possible that

Table 4.1: Purity and effective Hilbert space dimension of the reconstructed POVM elements of the 4-pixel SNSPD.

	Purity(π_n)	$M_{\text{eff}}(n)$
π_0	0.422744	2.3655
π_1	0.206398	4.84501
π_2	0.101156	9.88569
π_3	0.0427984	23.3653
π_4	0.0023035	434.121

multiple photons impinge on one pixel simultaneously, which as a result will only click once and thus is not inherently photon-number resolving. This behavior is reflected by the broadened distribution of the reconstructed POVMs in the photon number basis in Fig. 4.5 or equivalently the effective Hilbert space dimensions $M_{\text{eff}}(n) > 1$, which indicates that multiple orthogonal input states have significant contributions to a specific detection event. The extremely small purity or correspondingly high effective Hilbert space dimension for the “at least 4-click” POVM π_4 gives a perfect indication about the size of the detector array.

All input states larger than a specific threshold contribute to the highest measurement outcome, an “at least 4-click” event, since the device consists of only four pixels and thus can not resolve more than four impinging photons.

The reconstructed POVM matrix elements $\theta_i^{(n)}$ are the conditional probabilities

$$\theta_i^{(n)} = p(n \text{ clicks} | i \text{ incident photons}), \quad (4.6)$$

to receive an n -click event given i incident photons. Therefore, with the right definition, these reconstructed POVM elements can yield bounds on several detector figures of merit, such as efficiency η , dark-count probability p_{dark} and cross-talk probability p_{xtalk} . Note, all probabilities in the POVM matrix are given in “per pulse”, rather than “per second”.

4.3.2 Efficiency

The efficiency η of a detector can be defined as the probability that the detector responds with a click given that a single photon was incident. With the understanding that the POVM matrix elements are conditional probabilities, an intuitive equation for the efficiency can be formulated:

$$\eta = \sum_{n=1}^{N-1} p(n|1) = 1 - p(0|1), \quad (4.7)$$

where $N = 5$ is the total number of possible outcomes of the 4-pixel detector. The formula sums all probabilities that one or more clicks occur given one incident photon. Equivalently, since the probability that one of the possible outcomes occurs has to be equal to unity (which is also a constraint on the reconstruction in Eq. (2.16)), the counter-probability of the 0-click event can also be used for the calculation of the efficiency. With this definition, only a single POVM matrix element is necessary to determine the efficiency of the device using quantum detector tomography. The reconstruction yields a value of $p(0|1) = 0.37 \pm 0.04$, which results in an efficiency of $\eta = (63 \pm 4) \%$. The error stems from the uncertainty of the input state calibration, as mentioned in Section 4.3.1.

To validate this value, a separate experiment can be carried out to individually characterize the efficiency. In this experiment count rates from the 4-pixel SNSPD and a calibrated 1-pixel SNSPD with a known efficiency of $\eta_{\text{cal}} = (83 \pm 5) \%$ (compare Chapter 3) are recorded with a time tagger, for multiple input states. Afterwards, the mean photon numbers per pulse \bar{n}_{cal} are calculated from the count rates using Eq. (3.3) for the calibration detector. To calculate the mean photon numbers per pulse based on the count rates of the 4-pixel device, the formula

$$\bar{n}_{4\text{-pixel}} = -\ln\left(1 - \frac{\text{count rate}}{\text{rep. rate}}\right) \quad (4.8)$$

is used. Note, that this is the same formula as Eq. (3.3) except without the correction for the efficiency, as the efficiency of the device is still unknown. By dividing the calculated

mean photon numbers from the 4-pixel count rates by the mean photon numbers from the calibration detector count rates, the efficiency of the 4-pixel SNSPD can be calculated to

$$\eta = \frac{\bar{n}_{4\text{-pixel}}}{\bar{n}_{\text{cal}}} = (65 \pm 4) \% . \quad (4.9)$$

The uncertainty of this measurement is calculated using Gaussian error propagation and stems solely from the uncertainty of the efficiency of the calibration detector. The uncertainties on the count rates and the repetition rate are negligible and the standard deviation of the efficiencies between all measured input states is as low as 0.008, which means that the uncertainty cannot be improved by taking more data. The efficiency values from the individual characterization and the reconstruction are in good agreement, which validates the efficiency definition based on the reconstructed POVMs of the 4-pixel device.

4.3.3 Dark-Count Probability

As introduced in Section 2.1.3, dark counts are detection events that originate when no light is incident on the detector. Hence, the probability to receive a dark count corresponds to the conditional probability

$$p_{\text{dark}} = p(1|0) \quad (4.10)$$

and can directly be obtained from one matrix element of the reconstructed POVMs.

Smoothing Parameter Investigation

As mentioned in Section 4.2.3, previous work has shown that the reconstructed POVM elements are largely unaffected by the choice of the smoothing parameter γ [41]. However, the choice of an appropriate smoothing parameter is manifest in the dark-count probability estimation. The probability to receive a click when no photons are incident $\theta_0^{(1)}$ is expected to be very small, because of the typical low dark-count rates of SNSPDs. However, the probability of a click when one photon is incident $\theta_1^{(1)}$ is expected to be significantly larger, due to the relation of this element to the efficiency of the device (compare Eq. (4.7)), which is in the order of tenth of percent for SNSPDs. Figure 4.6(a) visualizes this difference between photon numbers $i = 0$ and $i = 1$ for the $n = 1$ event (red bars). In this special case, where two neighboring POVM elements are expected to vary by several orders of magnitude, an inopportune choice, that means choosing a smoothing parameter that is too large, can significantly overestimate the smaller of the two elements.

To illustrate the dependence on the smoothing parameter, Fig. 4.6(b) shows the “dark-count POVM element” $\theta_0^{(1)}$ as a function of the smoothing parameter γ . It is clear, that below a threshold of $\gamma = 0.17$ (vertical dashed line) the POVM element is independent on the choice of the smoothing parameter. However, above this threshold, all values for γ will lead to an overestimation of the dark-count probability $p_{\text{dark}} = p(1|0) = \theta_0^{(1)}$ of the device.

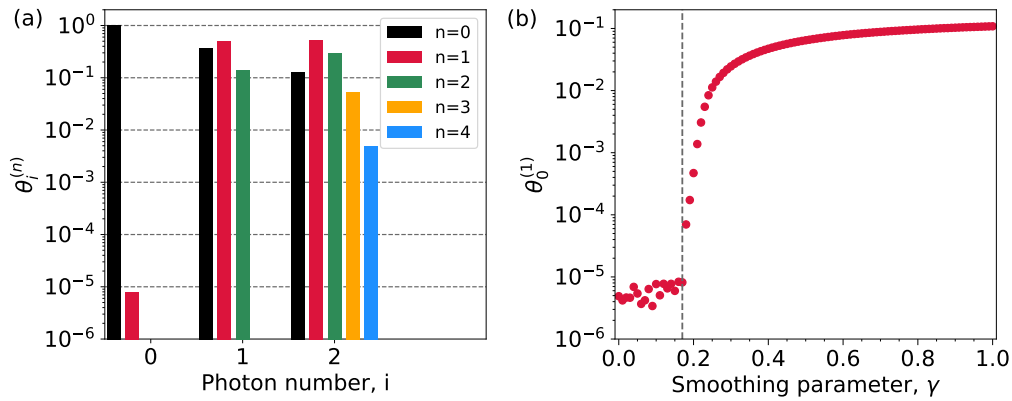


Figure 4.6: (a) Reconstructed POVM elements of the 4-pixel SNSPD (the same as in Fig. 4.5) on a logarithmic scale for the photon numbers up to $i = 2$, to visualize the difference in the magnitude of the probabilities. (b) Dependence of the $\theta_0^{(1)}$ POVM element (small red bar for $i = 0$ in (a)) on the smoothing parameter γ . For $\gamma > 0.17$ (indicated by the dashed line) the smoothing causes an overestimation of the given element.

To be below this threshold, the smoothing parameter was chosen to be $\gamma = 0.1$ for the main POVM reconstruction.

As the dark-count probability seems to vary slightly for smoothing parameters below the threshold of $\gamma = 0.17$, the mean value of all reconstructions for $\gamma \in [0, 0.17]$ in steps of 0.01 will be used to determine the dark-count probability of the 4-pixel SNSPD. This results in $p_{\text{dark}} = (5.9 \pm 1.6) \times 10^{-6}$. The error is determined by the standard deviation.

To validate the dark-count probability (per pulse) from the reconstruction, a separate dark-count measurement is carried out. For this experiment all input light gets blocked to the detector and a time tagger counts the number of times the detector clicks per second. This measurement reveals a dark-count rate of 211.3 dark counts per second. To be able to compare this value to the dark-count probability from the reconstructed POVMs, it has to be multiplied by the coincidence window used in the experiment, since this is the fraction of a second in which dark counts were measured per second and per pulse. For the uncorrelated dark counts, the coincidence window is 30 ns (compare Section 4.1), which results in $p_{\text{dark}} = (6.34 \pm 0.15) \times 10^{-6}$. The error stems from the Poisson error on the counting statistics, which resulted in a relative error of 2.29%. Both values from the individual measurement and the reconstruction are in good agreement. Note, that the uncertainty for the individual dark-count measurement is notably smaller, however, the advantage of quantum detector tomography is that one well-designed experiment is able to characterize the entire detector, thus multiple figures of merit at once.

4.3.4 Cross-Talk Probability

Cross-talk is a source of noise that has to be investigated for detector arrays. Especially, for the detector used in this thesis, which consists of four pixels that are wired in series (compare Fig. 2.3), cross-talk can lead to additional false detection events, as explained in Section 2.1.3.

Unlike dark counts, cross-talk is conditional noise, as additional counts can occur due to another pixel firing. Cross-talk is indicated by the significantly larger probability $p(2|1)$ (two clicks given one incident photon) compared to the probability $p(1|0)$ (two clicks given one incident photon) in Fig. 4.6, which can only be explained by some additional noise source increasing this probability. However, cross-talk manifests itself most clearly in the occurrence of contributions to the probability distribution for photon numbers $i < n$, as indicated by the red bars in Fig. 4.7(c)-(e). Note, that for an ideal detector (no cross-talk), these contributions are impossible, since e.g. a single photon can not cause a two click event, as it is absorbed by the detector material upon impinging on the first pixel or in general, it is not physically possible that i photons can cause n clicks for $i < n$.

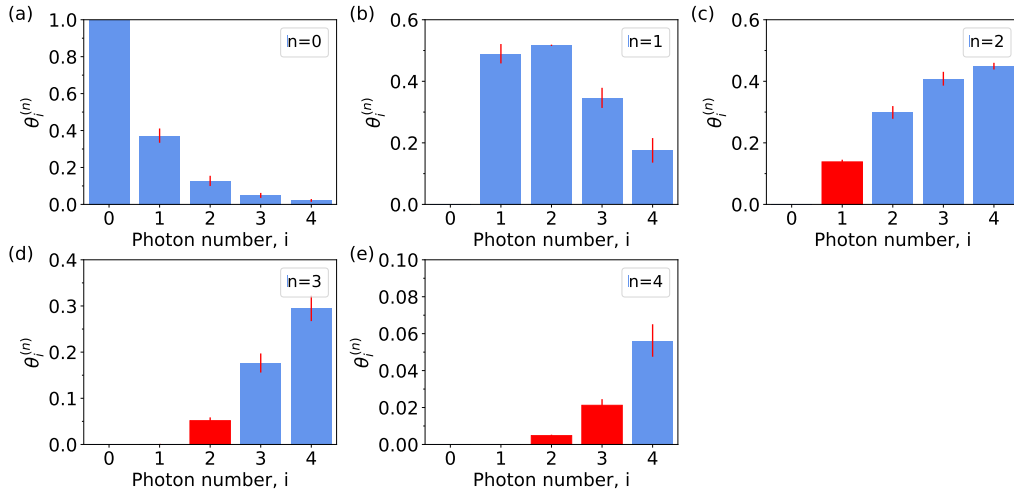


Figure 4.7: Reconstructed POVM elements up to a photon number of $i = 4$, displayed in a bar graph per outcome n . The effect of cross-talk is shown through contributions from photon numbers $i < n$ to the click-events n (marked by the red bars).

In principle, cross-talk will affect POVM elements $p(n|i)$, for $n > \max(i, 1)$ when disregarding loss and $p(n|i)$, for $n > 1$ when including loss. Focusing on the element $p(2|1)$ (two click given one incident photon) it is possible to find an intuitive definition for the single-pixel cross-talk probability of the device as

$$p_{\text{xtalk}} = p(2|1) - p(1|1)p(1|0). \quad (4.11)$$

The reason behind this is, that in the absence of cross-talk, the case of two clicks given one incident photon ($p(2|1)$) can only be caused by one incident photon causing a click ($p(1|1)$) and an additional dark count arising from the remaining pixels ($p(1|0)$). Any additional counts in this scenario are attributed to cross-talk.

Following this definition and with $p(2|1) = 0.14 \pm 0.01$, $p(1|1) = 0.49 \pm 0.03$ and $p(1|0) = p_{\text{dark}} = (5.9 \pm 1.6) \times 10^{-6}$, the cross-talk probability of the 4-pixel SNSPD can be estimated by $p_{\text{xtalk}} = (14 \pm 1) \%$.

A 14 % probability of an additional pixel firing due to a detection event on another pixel is fairly high. To improve detector arrays in general and thus decrease the cross-talk probability, several possibilities can be considered. A long bias plateau in combination with very pronounced voltage thresholds for the individual outcomes, or better (low-noise) amplifiers or even low-temperature amplifiers would enable an operation of the detector at lower bias currents. As cross-talk is caused by small current density fluctuations, a lower bias current further away from the critical current of the superconducting nanowire can significantly decrease the probability of cross-talk events. An optimization of the detector geometry can also be beneficial.

Although, the 4-pixel SNSPD has a long bias plateau (compare Fig. A.1) the bias current I_{bias} was chosen very close to the critical current, which can certainly lead to an increased cross-talk probability. However, a trade off between a high bias current and well pronounced threshold levels was made to improve the differentiation of different click events and thus lead to a more accurate measurement at the cost of an increased cross-talk probability.

As already indicated in Section 2.1.3, the task of independently measuring or modeling cross-talk is challenging, as it depends on the total number of pixel, the number and location of remaining pixels after a detection event and correlations between pixels, which ultimately needs recourse to the underlying working principle and geometry of the device [46–53]. The complexity of an underlying model can be illustrated using merely the probability $p(2|2)$, as there are multiple combinations that would contribute to this element:

- two photons impinge, both cause a click
- two photons impinge, one photon gets lost, the other one causes cross-talk
- two photons impinge, one photon gets lost, a dark count causes another click
- two photons impinge, both get lost, two dark counts cause two clicks
- two photons impinge, both get lost, a dark count causes cross-talk

Nevertheless, the aim of this section is to provide an intuitive and straightforward estimate of the cross-talk probability of detector arrays, which certainly serves as a useful characteristic of the device. This estimate could for example be used as a figure of merit to directly compare and possibly classify commercially available detector arrays.

4.3.5 Detector Wigner Functions

Besides determining detector figures of merit, the POVM operators π_n can also be used to visualize detection outcomes in phase space using the Wigner function representation. Figure 4.8(a)-(e) shows Wigner functions for the five possible outcomes of the 4-pixel SNSPD.

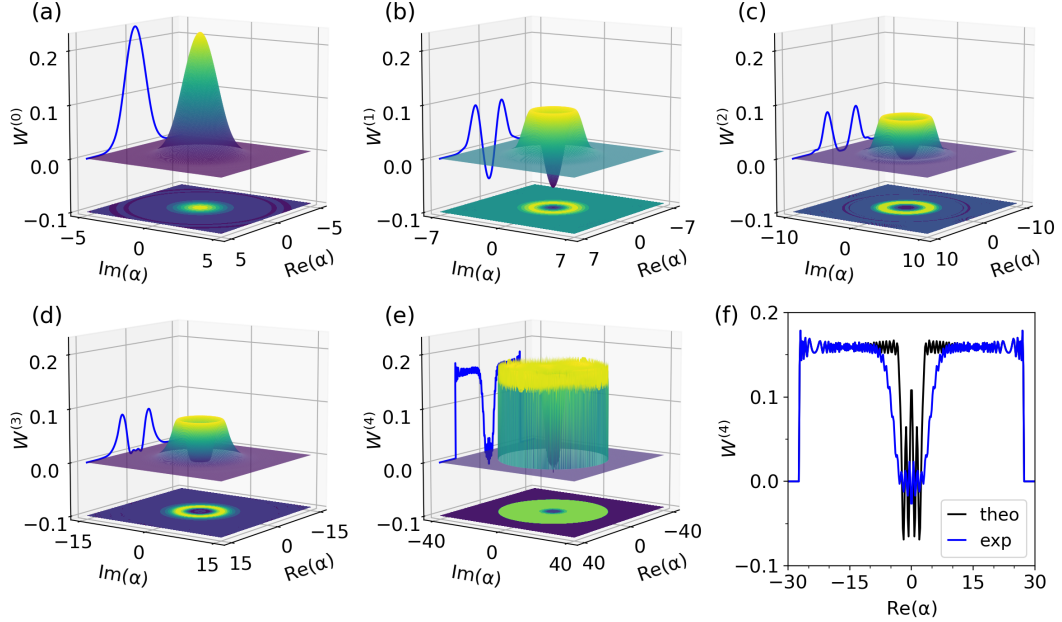


Figure 4.8: (a)-(e) Wigner functions of the five possible outcomes of the 4-pixel SNSPD, directly calculated from the POVM operators π_n . Negativity indicates non-classicality, which classifies this detector as a quantum detector that can detect non-classical optical states. (f) Comparison of the “at least 4-click” POVM π_4 of the 4-pixel SNSPD (blue) and the density matrix $\rho_4 = \mathbb{1} - |3\rangle\langle 3| - |2\rangle\langle 2| - |1\rangle\langle 1| - |0\rangle\langle 0|$ (black), which is a theoretical description of the “at least 4-click” event. The cut contains all information, as the Wigner functions show rotational symmetry, due to phase-insensitivity of the 4-pixel SNSPD.

The detector Wigner functions for events $n \leq 3$ show close resemblance to those of Fock states, which confirms the capability of the 4-pixel SNSPD as a photon-number resolving detector in the non-saturated regime [39]. The resemblance stems from the fact that the density matrix of Fock state $|n\rangle$ is given by $\rho_n = |n\rangle\langle n|$ and a perfect quantum mechanical measurement of an n -click event is also described by the density matrix $\rho_{n\text{-click}} = |n\rangle\langle n|$. The 0-click Wigner function $W^{(0)}$ is broadened compared to the vacuum state $|0\rangle\langle 0|$, as losses increase the sensitivity of the 0-click event to higher photon numbers. The clear negativity at the origin of the 1-click Wigner function $W^{(1)}$ indicates the absence of a classical optical analogue. Hence, this device is a fundamental quantum detector with the ability to detect non-classical optical states [39].

The rotational symmetry of the Wigner functions around the origin stem from the phase-insensitivity of the 4-pixel SNSPD. The “at least 4-click” Wigner function of the device is distinctly different compared to the other events. This is already explained by the use of the term “at least”. The detection event is not described by the density matrix $|4\rangle\langle 4|$, but rather by $\rho_4 = \mathbb{1} - |3\rangle\langle 3| - |2\rangle\langle 2| - |1\rangle\langle 1| - |0\rangle\langle 0|$, as the detector can not distinguish between four or more than four photons. Figure 4.8(f) shows a comparison of the detector Wigner function based on the reconstructed POVM π_4 and the Wigner function for ρ_4 . The matching shape of the distributions validates the theoretical description of the “at least 4-click” detector outcome. However, ρ_4 does not account for loss or noise such as dark-counts and cross-talk. Accounting for those, may improve the match between the curves. Note that the end ripples in Fig. 4.8(f) are an edge effect caused by number state cutoff [41].

4.3.6 Convergence and Sanity Check

The definitions for the three main detector figures of merit: efficiency, dark-count probability and cross-talk probability, only depend on four matrix elements of the reconstructed POVM Π (compare Sections 4.3.2-4.3.4). Additionally, these elements only depend on the photon numbers $i = 0$ and $i = 1$ in the POVM matrix Π , which rises the question, whether it is possible to receive the crucial elements from fewer states with lower mean photon numbers per pulse.

This section aims to find the minimum number of states and the lowest mean photon number necessary that reliably determine the four elements corresponding to the probabilities $p(1|0)$, $p(0|1)$, $p(1|1)$ and $p(2|1)$. This information is important, when applying quantum detector tomography to considerably larger detector arrays, since for increasing detection outcomes N , states D and mean photon numbers per pulse to saturate the detector and span the Hilbert space dimension M of the device, the reconstruction time and the demand for computing power will also increase.

First, the meticulous choice of the truncation of the coherent state expansion i.e. the Hilbert space dimension M in Section 4.2.1 will be investigated. To do that, the POVM matrix Π will be reconstructed multiple times following the standard procedure from Eq. (2.16) with varying Hilbert space dimensions M . Figure 4.9 shows the four POVM elements corresponding to the probabilities $p(0|1)$, $p(1|0)$, $p(1|1)$ and $p(2|1)$ as a function of the Hilbert space dimension M . All four elements converge for Hilbert space dimensions $M > 400$, which shows the importance of choosing an appropriate value for the truncation of the coherent state expansion in the photon number basis. Furthermore, this confirms the selection of including probability amplitudes six standard deviations greater than the largest coherent state in the coherent input state matrix \mathbf{F} (compare Section 4.2.1), as all meaningful contributions to the probability distribution are included and no degradation to the description of the coherent states can be noticed.

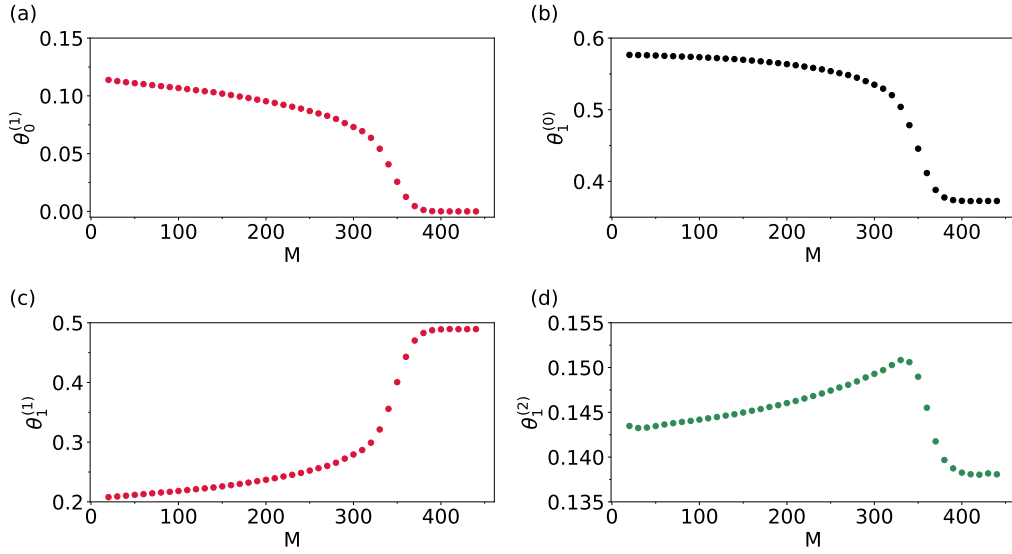


Figure 4.9: POVM elements corresponding to the probabilities $p(0|1)$, $p(1|0)$, $p(1|1)$ and $p(2|1)$ (from top left to bottom right) as a function of the Hilbert space dimension M .

Afterwards, the dependency of the four important POVM matrix elements on the number of coherent input states D , with that the size of the largest coherent state $|\alpha|^2$, will be examined. In the experiment, the mean photon numbers of the coherent states were chosen to scale approximately quadratically $|\alpha_d|^2 \approx d^2$ with $d \in [0, D-1]$. By performing multiple reconstructions of the POVM matrix $\mathbf{\Pi}$, further truncating the number of input states D for each reconstruction, the effect on the POVM elements can be investigated. The Hilbert space dimension M for a specific reconstruction will be adjusted according to the current number of input states D , which determines the mean photon number of the largest coherent state.

To visualize the results of the different reconstructions, the relative deviation of the POVM elements to those of the full reconstruction (compare Section 4.3.1)

$$\delta\theta_i^{(n)} = \frac{|\theta_i^{(n)} - \theta_{i,\text{full}}^{(n)}|}{\theta_{i,\text{full}}^{(n)}} \quad (4.12)$$

is plotted against the number of coherent input states D (Fig. 4.10). Except the dark-count POVM element $\theta_0^{(1)}$, the other three probabilities show convergence with very low relative deviations at $D = 6$ coherent input states. This corresponds to a mean photon number of $|\alpha_5|^2 \approx 25$ for the largest necessary coherent state and a Hilbert space dimension of $M = 55$. The reason that the element $\theta_0^{(1)}$, shown in Fig. 4.10(a), does not converge is that the amplitude of this element is in the order of 10^{-6} , which means that even the slightest variations will cause significant relative deviations although the order of magnitude is

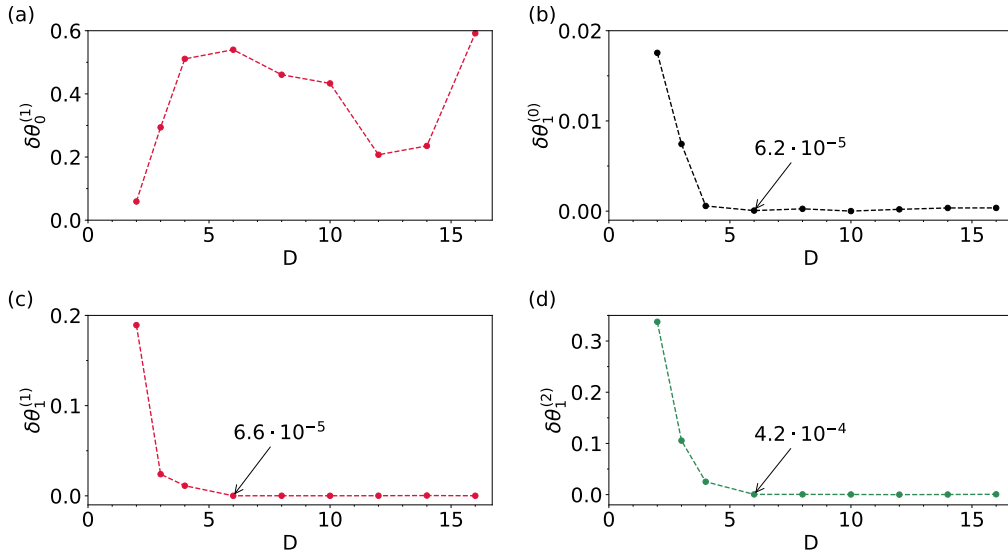


Figure 4.10: Relative deviation $\delta\theta_i^{(n)}$ of the four important POVM elements (corresponding to the probabilities $p(0|1)$, $p(1|0)$, $p(1|1)$ and $p(2|1)$) to those of the full reconstruction in Section 4.3.1 as a function of the total number of coherent input states D .

unchanged. The results indicate that the three main figures of merit: efficiency, dark-count probability and cross-talk probability for this specific device (the 4-pixel SNSPD) can be determined with high accuracy, compared to the full reconstruction, from merely six coherent input states with mean photon numbers of $|\alpha|^2 \approx 0, 1, 4, 9, 16$ and 25. A fidelity (Eq. (2.18)) of $\mathcal{F} \geq 99.8\%$ for all outcomes n reveals an almost perfect match between the adjusted POVM and the full POVM, when truncating both matrices at $M = |\alpha_5|^2 = 25$. The choice of this truncation is explained by the fact that the POVM elements π_n are not representative for photon numbers i that exceed the largest mean photon number $|\alpha_{d_{\max}}|^2$, as no detector response has been measured for these photon numbers (see the following section for further details).

The full reconstruction of the POVM elements of the 4-pixel detector, that means the execution time of the entire *Python*-function took roughly 8 s. Reducing the number of input states D , thus the Hilbert space dimension M (compare Fig. 4.10) and plotting the calculation time against the total number of POVM matrix elements $N \cdot M$, which is the number of variables in the reconstruction, revealed a linear dependency (compare Fig. A.2 in the appendix). In Fig. 4.10 it was found that the “truncated reconstruction” for merely $D = 6$ coherent input states (and a corresponding Hilbert space dimension of $M = 55$) revealed very small deviations from the full reconstruction of the POVM matrix $\mathbf{\Pi}$ with a fidelity of almost unity. The time for this reconstruction was merely 0.9 s, resulting in an eight times faster calculation. All reconstructions were executed on a standard desktop computer with 16 GB RAM and no computational effort could be noticed.

The calculations in this section do not allow for any generalization for other detectors as they may be inherently different. However, it does show that characterizing the figures of merit of larger detector arrays through quantum detector tomography is in principle possible without the need to saturate the device or span the entire Hilbert space, which will ultimately save valuable calculation time and computing power.

Sanity Check

Although, it is reasonable to assume that post saturation of the largest POVM π_4 this element stays saturated, as more photons will also always lead to a 4-click event, this behavior is not guaranteed, as too much impinging light may cause the detector to latch and thus making it unable to detect subsequent photons. Only photon numbers for which a detector response was measured can be correctly represented by the POVMs. This can be visualized by performing a non-smoothed ($\gamma = 0$) reconstruction of the matrix Π and plotting the entire matrix up to $i = 443$ (Fig. 4.11). It can be seen, that all POVM elements

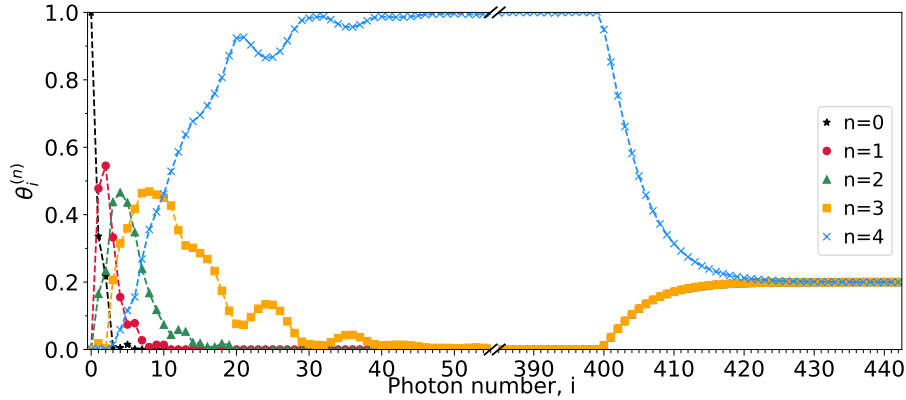


Figure 4.11: Reconstructed POVM elements π_n of the 4-pixel detector with no smoothing applied ($\gamma = 0$). Due to the lack of smoothing, the POVM elements do not follow a smooth distribution (compared to Fig. 4.5). A convergence to $\frac{1}{N}$ can be noticed for large photon numbers i .

π_n converge to a value of $\frac{1}{N} = 0.2$, where N is the number of outcomes for the 4-pixel SNSPD. This is explained by a lack of information for large photon numbers i , since the sum of the Poisson distributions of the coherent states in the input state matrix \mathbf{F} rapidly decreases after the largest coherent state, since there are no further states (compare Fig. 4.3). Due to this lack of information, the reconstruction is not able to assign a photon number to a detection outcome and therefore making each outcome equally likely. This sanity check confirms the fact, that the POVM elements π_n are only representative for photon numbers with significant contributions in the coherent states that were measured in the experiment.

Detector Tomography:

4-Bin Detector

5

In this chapter quantum detector tomography is applied to another type of detector, a 4-bin spatially multiplexed detector. This device enables a validation of the cross-talk probability definition from Section 4.3.4. In principle, this detector design should not show any signs of cross-talk between detectors, as it consists of four separate devices each current biased and read out individually. Therefore, the cross-talk probability p_{xtalk} should equal zero. Although, it should be mentioned, that since the detectors are located in the same cryostat and use a common ground, some unwanted connection between the devices is possible, for example in the amplification of the detector signals.

5.1 Experimental Setup

First, the coherent input states need to be calibrated to find their mean photon numbers. The calibration procedure is described in Chapter 3. Afterwards, the 4-bin detector measurement can be carried out. The experimental setup is shown in Fig. 5.1. Just like the input state calibration measurement and the 4-pixel detector tomography measurement, a 1556 nm pulsed laser generates coherent states at 500 kHz, which can be attenuated by two computer controlled variable optical attenuators. The input states are split into four channels via three 50:50 beam splitters. Before impinging on the detectors, the polarization can be controlled separately in each channel. This is important, as each SNSPD is optimized for a slightly different polarization. The output pulses of the detectors are measured in synchronization with the laser pulses in a 10 ns coincidence window using a time tagger. The detectors used for this measurement are three 1-pixel SNSPDs and the 4-pixel SNSPD (read out at the 1-click threshold), all located in a cryostat at 0.8 K. The optimal bias currents I_{bias} , voltage thresholds and artificial dead times (to avoid triggering on noise on the falling edge of the output pulse) can be found in Table A.3.

With this detection scheme, there are multiple combinations for different n -click events. For example for a 4-bin detector, there are four possibilities, that one click occurs (as each detector can click independently), but only one case where four clicks occur (as all detectors need to click simultaneously). For a j -bin detector the formula to calculate the number of possible combinations of click events n (without the $n = 0$ or no-click event) is:

$$C = \sum_{n=1}^j \binom{j}{n} = \sum_{n=1}^j \frac{j!}{n!(j-n)!} = 2^j - 1. \quad (5.1)$$

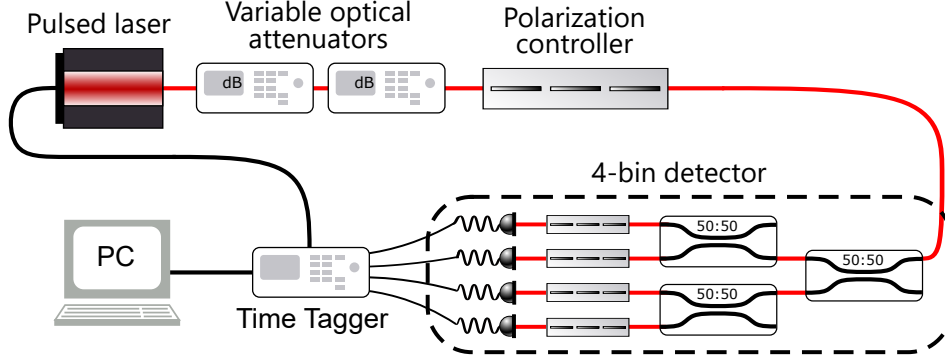


Figure 5.1: Experimental setup for the 4-bin detector tomography experiment. The 4-bin spatially multiplexed detector consists of four individual detectors all located in a cryostat at 0.8 K. A 1556 nm pulsed laser generates coherent states at 500 kHz, which can be attenuated before being split into the four detection channels. A time tagger synchronized with the laser pulses will measure the outcome statistics of the 4-bin device.

For $j = 4$ bins, that calculates to $C = 15$ different combinations. Therefore 15 coincidence count rates (four 1-click cases, six 2-click cases, four 3-click cases and one 4-click case) are measured with the time tagger all in coincidence with the laser pulses.

Similar to the 4-pixel SNSPD detector tomography experiment, the states are chosen to scale approximately quadratically $|\alpha_d|^2 \approx d^2$ with $d \in [0, 11]$, resulting in photon number distributions from 0 to 122 photons per pulse, which span the entire Hilbert space of the detector. Compared to the 4-pixel detector, fewer and therefore smaller coherent states are sufficient, as the 4-bin detector shows a saturation of the 4-click event for a mean photon number of $|\alpha_{11}|^2 \approx 122$ per pulse. Each coherent input state is measured for 10 s or equivalently 5×10^6 times to achieve sufficient statistics. As explained in Section 4.1, the 0-photon input state, also called dark-count measurement, is measured for 600 s for sufficient statistics, as the dark-count rates for SNSPDs are very low.

5.2 Analysis

To perform detector tomography and reconstruct the POVM elements of the 4-bin detector, the measurement statistics matrix \mathbf{P} and the coherent input state matrix \mathbf{F} need to be constructed from the experimental results and the mean photon numbers used in the experiment, respectively.

5.2.1 Coherent Input State Matrix

The coherent input state matrix \mathbf{F} for the $D = 12$ input states is constructed in the same procedure as explained in Section 4.2.1. However, a new input state calibration was performed

prior to this measurement, therefore, the fit parameters to calculate the mean photon numbers per pulse \bar{n} from the attenuations α in the experiment are slightly different. The y-axis intercept is $b = 4.371_{-0.025}^{+0.027}$ and the slope of the linear fit is $m = -0.09844 \pm 0.00009$. The attenuations and mean photon numbers for this experiment can be found in Table A.4.

5.2.2 Measurement Statistics Matrix

The 4-bin spatially multiplexed detector has $N = 5$ possible outcomes. However, unlike the 4-pixel SNSPD, the analysis to arrive at the exact n -click count rates c'_n and thus the measurement statistics matrix \mathbf{P} is slightly more involved. Due to the data acquisition, the resulting 15 different coincidence count rates are non-orthogonal outcomes, meaning that for example a coincidence count between all four detectors A, B, C and D will also be measured as a coincidence count between all combinations of three detectors, two detectors and one detector. This also applies to other coincidence count rates, for example a coincidence count between detectors A, B and C (here indexed with c_{ABC}) will also trigger a coincidence count in all combinations of two of these detectors, such as c_{AB} , c_{AC} and c_{BC} . With this in mind, the first step is to transform the “at least” count rates c to “exact” count rates c' .

The “at least 4-click” count rate will stay unchanged, since it is not possible to distinguish between four or more than four photons with a 4-bin multiplexed detector:

$$c'_{ABCD} = c_{ABCD}. \quad (5.2)$$

The four different 3-click coincidence count rates will be calculated by subtracting the “at least 4-click” count rate:

$$c'_{ABC} = c_{ABC} - c_{ABCD} \quad (5.3a)$$

$$c'_{ABD} = c_{ABD} - c_{ABCD} \quad (5.3b)$$

$$c'_{ACD} = c_{ACD} - c_{ABCD} \quad (5.3c)$$

$$c'_{BCD} = c_{BCD} - c_{ABCD}. \quad (5.3d)$$

The reason is that every “at least 3-click” count rate contains the “at least 4-click” count rate, which means that it is increased by the amount of the “at least 4-click” count rate.

This also applies to the 2-click events. Hence, the formulas for those events will include a subtraction of the “at least 4-click” count rate as well. Additionally, the calculation will include a subtraction of the correct 3-click count rates, using the same argumentation as for the 3-click count rates (every time a coincidence is measured between any three detectors also a coincidence between two of the involved detectors will be counted). Therefore, when calculating for example the 2-click count rate c'_{AB} the 3-click count rates jointly containing the detectors A and B need to be subtracted from the “at least 2-click count rate” (care must be taken to ensure not to subtract the “at least 4-click” count rate twice, therefore it

is advised to always subtract the non-transformed count rates c):

$$c'_{AB} = c_{AB} - c'_{ABC} - c'_{ABD} - c_{ABCD} \quad (5.4)$$

Substituting in the correct equation from Eq. (5.3) and applying it also to the remaining five 2-click coincidence events leads to the following equations:

$$c'_{AB} = c_{AB} - c_{ABC} - c_{ABD} + c_{ABCD} \quad (5.5a)$$

$$c'_{AC} = c_{AC} - c_{ABC} - c_{ACD} + c_{ABCD} \quad (5.5b)$$

$$c'_{AD} = c_{AD} - c_{ABD} - c_{ACD} + c_{ABCD} \quad (5.5c)$$

$$c'_{BC} = c_{BC} - c_{ABC} - c_{BCD} + c_{ABCD} \quad (5.5d)$$

$$c'_{BD} = c_{BD} - c_{ABD} - c_{BCD} + c_{ABCD} \quad (5.5e)$$

$$c'_{CD} = c_{CD} - c_{ACD} - c_{BCD} + c_{ABCD} . \quad (5.5f)$$

The same procedure applies for the transformation of the 1-click count rates which will ultimately be calculated as follows:

$$c'_A = c_A - c_{AB} - c_{AC} - c_{AD} + c_{ABC} + c_{ABD} + c_{ACD} - c_{ABCD} \quad (5.6a)$$

$$c'_B = c_B - c_{AB} - c_{BC} - c_{BD} + c_{ABC} + c_{ABD} + c_{BCD} - c_{ABCD} \quad (5.6b)$$

$$c'_C = c_C - c_{AC} - c_{BC} - c_{CD} + c_{ABC} + c_{ACD} + c_{BCD} - c_{ABCD} \quad (5.6c)$$

$$c'_D = c_D - c_{AD} - c_{BD} - c_{CD} + c_{ABD} + c_{ACD} + c_{BCD} - c_{ABCD} . \quad (5.6d)$$

Finally, to calculate the “exactly” n -click count rates c'_n , all possible n -click count rates need to be added together:

$$c'_1 = c'_A + c'_B + c'_C + c'_D \quad (5.7a)$$

$$c'_2 = c'_{AB} + c'_{AC} + c'_{AD} + c'_{BC} + c'_{BD} + c'_{CD} \quad (5.7b)$$

$$c'_3 = c'_{ABC} + c'_{ABD} + c'_{ACD} + c'_{BCD} \quad (5.7c)$$

$$c'_4 = c_{ABCD} . \quad (5.7d)$$

The no-click or 0-click event is calculated by subtracting the sum of all other count rates from the repetition rate of the laser (again labeled as the “at least 0-clicks” c_0). This is possible, since all laser pulses that did not lead to any click event are considered to be a no-click event.

Ultimately, to construct the measurement statistics matrix \mathbf{P} the transformed count rates are divided by the repetition rate of the laser c_0 . Hence, the matrix elements are given by

$$P_{d,n} = \left. \frac{c'_n}{c_0} \right|_d . \quad (5.8)$$

5.2.3 POVM Reconstruction

With the coherent input state matrix \mathbf{F} and the measurement statistics matrix \mathbf{P} the POVM elements of the 4-bin spatially multiplexed detector can be reconstructed. The reconstruction of the POVM operators follows the exact same procedure as for the 4-pixel detector (compare Section 4.2.3).

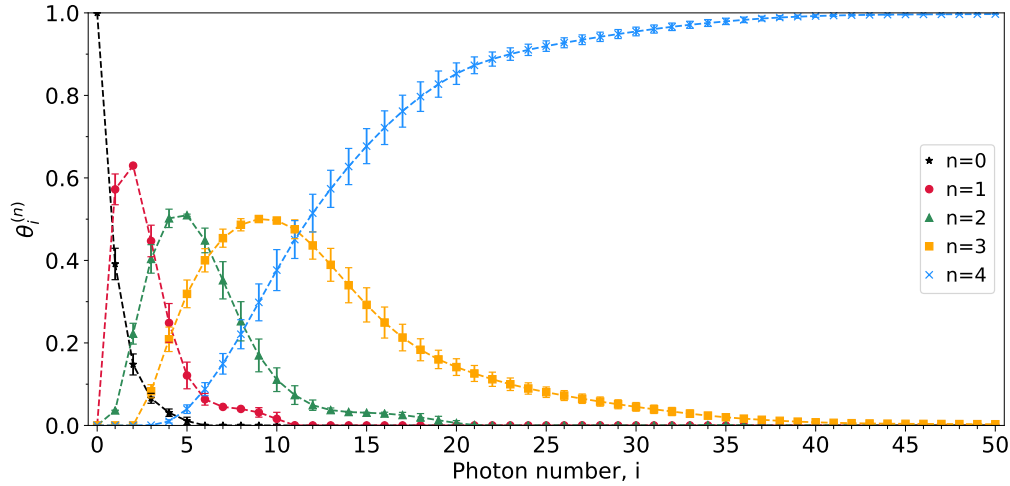


Figure 5.2: Diagonal elements of the reconstructed POVM operators π_n of the 4-bin spatially multiplexed detector in the photon number basis shown up to a photon number $i = 50$. All outcomes show the expected smooth distribution. The error bars stem from the 5% uncertainty on the efficiency of the calibration detector.

5.3 Results

The reconstructed POVM elements π_n of the 4-bin detector show the expected smooth distribution for lossy detectors (Fig. 5.2). Analyzing the POVM operators in same procedure as for the 4-pixel detector, reveals the figures of merit of the device (Table 5.1 and Table 5.2). The dependency of the dark-count POVM element $\theta_0^{(1)}$ from the smoothing parameter γ is the same as in Fig. 4.6(b). Therefore, p_{dark} is again calculated as the mean value of all reconstructions below the threshold of $\gamma = 0.16$ and the uncertainty is determined by the standard deviation.

The efficiency and the dark-count probability of the 4-bin detector are very similar to those of the 4-pixel device. This is sensible, since the 4-bin device consists of three 1-pixel SNSPDs and the 4-pixel SNSPD (read out at the “at least 1-click” threshold) and all devices have low dark-count rates. The Purity(π_n) and the effective Hilbert space dimension $M_{\text{eff}}(n)$ show close resemblance to the values of the 4-pixel SNSPD, note that the maximum Hilbert space for the 4-bin device was $M = 189$. The similarity can be attributed to the fact that both

detectors are not inherently photon-number resolving, which leads to multiple orthogonal input states contributing to the same detection event.

Table 5.1: Efficiency, dark-count probability and cross-talk probability of the 4-bin detector.

η	$(61 \pm 4) \%$
p_{dark}	$(5.4 \pm 1.8) \times 10^{-4} \%$
p_{xtalk}	$(3.6 \pm 0.1) \%$

Table 5.2: Purity and effective Hilbert space dimension of the 4-bin detector.

	Purity(π_n)	$M_{\text{eff}}(n)$
π_0	0.422694	2.36578
π_1	0.201214	4.96983
π_2	0.104094	9.60669
π_3	0.0476509	20.986
π_4	0.0055903	178.881

As mentioned in the beginning of this chapter, this experiment was mainly performed to confirm the cross-talk probability definition from Section 4.3.4. In principle, this detector design should not show any cross-talk between the separate detectors. This is partially confirmed by the non-existing or significantly lower contributions from photon numbers $i < n$ in Fig. 5.3, which compares the POVM elements of the 4-pixel SNSPD to the 4-bin detector up to a photon number of $i = 4$.

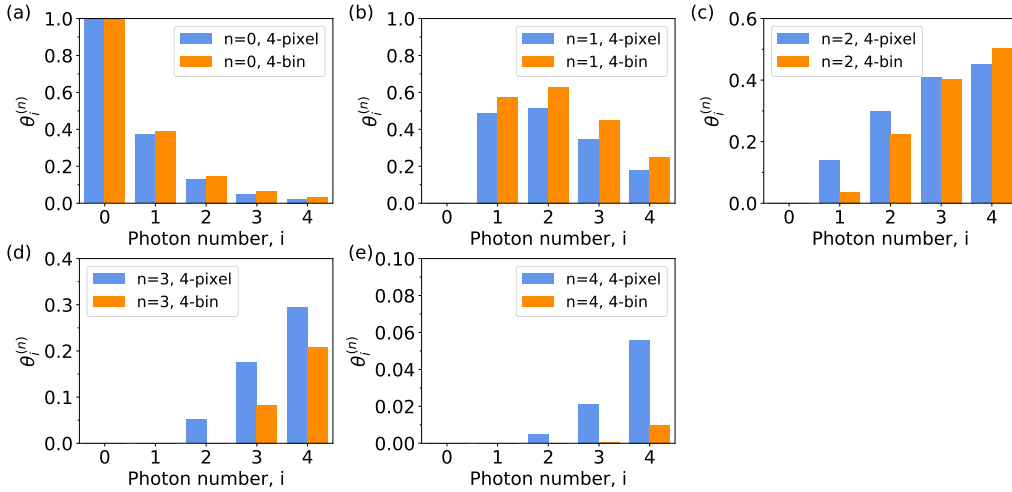


Figure 5.3: Comparison of the 4-pixel POVM elements (blue) and the 4-bin POVM elements (orange) up to a photon number of $i = 4$. Contributions from photon numbers $i < n$ indicate cross-talk.

However, utilizing Eq. (4.11) with the probabilities $p(2|1) = 0.036 \pm 0.001$, $p(1|1) = 0.57 \pm 0.03$ and $p(1|0) = p_{\text{dark}} = (5.4 \pm 1.8) \times 10^{-6}$ from the reconstruction, the cross-talk probability of the 4-bin detector can be estimated by $p_{\text{xtalk}} = (3.6 \pm 0.1) \%$. The calculation is dominated by the probability $p(2|1)$, as the dark-count probability of the device is negligible.

The non-zero cross-talk probability contradicts the assumption that this device should not show any cross-talk between the individual detectors. One explanation stems from the fact that there could possibly be a connection between some of the detectors, as they are located in the same cryostat and use a common ground. This theory is tested by disabling each detector one by one in the post processing, thus turning the 4-bin detector into four possible 3-bin detectors. This can be done by manually setting the count rate and the coincidence rates to zero, which contain the specific detector. This method allows to seek out the a possible connection between two of the detectors, as the cross-talk probability should be zero for the 3-bin detectors which are missing the troublesome connection. Unfortunately, by repeating the POVM reconstruction for each 3-bin detectors, the cross-talk probabilities are still non-zero, although they have decreased to $< 1\%$.

To extend the initial theory, there could also exist a connection between three of the detectors. This is tested by disabling two detectors each time, enabling six 2-bin detectors. Although, once again decreased to $< 0.17\%$, all cross-talk probabilities remain non-zero, which almost certainly refutes the theory of an existing connection between the detectors unless there is a correlation between all four detectors. However, by following this procedure and disabling three detectors at once, it is not possible to test this. A 1-bin or 1-pixel detector cannot show cross-talk, since there is no second detector that may fire as a result of an initial detection event. The results from the POVM reconstruction of a time-multiplexed detector in Section 6.3.3 yield more insight about cross-talk.

Another explanation for the non-zero cross-talk probability stems from a result from Section 4.3.6. It was shown that the POVM matrix element corresponding to the probability $p(2|1)$ only depends on small coherent input states, as the relative deviation $\delta\theta_1^{(2)}$ between the “truncated reconstruction” based on merely $D = 6$ input states and the full reconstruction is very small. However, if the uncertainty in the input state calibration is larger than expected, it could lead to non-ideal states and thus an increased uncertainty in the entire reconstruction. This theory has to be tested by meticulously choosing the input states, preferably with an increased precision. Especially coherent states with a mean photon number of $|\alpha|^2 \approx 1$ or even single-photon Fock states can be utilized to examine cross-talk more closely. With these input states cross-talk would be most notable in an elevated 2-click count rate, although mostly only one or exactly one (for the Fock state) photon is incident on the device.

Scalability of Detector Tomography

6

Section 4.3.6 showed that it is possible to determine the main figures of merit of detector arrays without saturating them and thus without spanning their entire Hilbert space. This opens up the possibility to apply detector tomography to larger detector arrays and characterize them. However, one question that still remains is, how large the devices can be until the current tomographic reconstruction gets to demanding regarding computation time and cost. To test the tomographic reconstruction for increasing detector sizes, which means increasing number of outcomes, a time-multiplexed detector (TMD) is utilized [34]. This design is in principle not saturable as the number of time bins is not fixed and can be chosen to be very large. Therefore, this detector is optimal to demonstrate the scalability of quantum detector tomography and the reconstruction process.

6.1 Introduction: Loop-Detector Design

This time-multiplexed detector design enables the detection of single photons as well as bright light. It is comprised of a variable beam splitter with one output connected to one input and the other output connected to a single-photon detector, in this case a 1-pixel SNSPD (Fig. 6.1). Pulses from a light source will enter the beam splitter loop and are then split into smaller sub-pulses each separated by the loop length of $\tau = 156$ ns. It is important to ensure that the dead time of the detector is much shorter than the loop length τ , otherwise some sub-pulses could not be detected or the detector could enter the latched state, where it is insensitive to any subsequent photons. The sub-pulses, which are always some fraction of the light remaining in the loop, are detected from the detector in a series

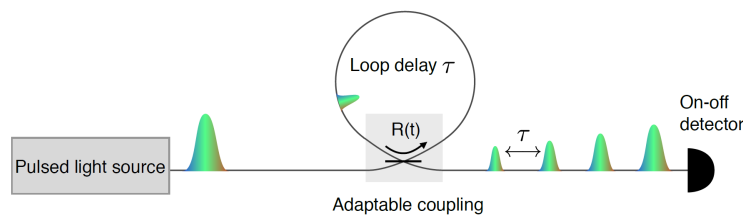


Figure 6.1: Click-detector connected to a variable beam splitter of which one output and one input form a loop. The pulses from a light source are split into smaller sub-pulses that are delayed by the loop length τ and detected by the click-detector (from [34]).

of time bins j . The probability that a certain bin j clicks for coherent input states is:

$$p_j^{\text{coh}} = \begin{cases} 1 - (1 - \nu)\exp[-R\bar{n}] & , j = 1 \\ 1 - (1 - \nu)\exp[-(1 - R)^2 R^{-1}(\eta R)^{j-1} \bar{n}] & , j \geq 2, \end{cases} \quad (6.1)$$

where ν is a constant dark-count probability (noise floor) for each bin, R is the coupling constant of the beam splitter, which determines the fraction of light that gets coupled onto the detector, \bar{n} is the mean photon number per pulse generated by the light source and η_{loop} is the loop efficiency, which determines the losses in each round trip of the loop [34].

6.2 Simulation

A simulation is carried out in preparation of the detector tomography experiment of the time-multiplexed detector. With this simulation it is possible to assess how an outcome should be defined, how many outcomes should be used and how large the mean photon number needs to be to saturate all detection outcomes.

The definition of an outcome is crucial, as it determines the necessary steps in the analysis of the data. As mentioned in the previous section, this device detects sub-pulses, created from one coherent input state, in time bins j which are separated by the loop length τ . The first logical definition of an outcome could be: what is the probability that bin j clicks. This would also be the simplest definition to measure in an experiment. For this a histogram, containing a certain number of bins spaced according to the loop length τ , needs to be recorded in response to multiple copies of the same state (to acquire sufficient statistics). By normalizing the histogram to the total number of incident states the measurement statistics matrix \mathbf{P} can be constructed. Another definition of an outcome could be that a given combination of multiple bins click.

However, to define an outcome as the number of clicks caused by the sub-pulses from one incident coherent state (at the beam splitter loop) would allow for a direct comparison to the other detectors used in this thesis, the 4-pixel SNSPD and the 4-bin spatially multiplexed detector. Hence, this is the definition of choice.

6.2.1 Matrix-Construction

The simulation of the measurement statistics matrix $\mathbf{P}_{D \times N}$ with outcomes (n -clicks occur) as columns for different coherent input states as rows is based on Eq. (6.1), which describes the probability that a specific bin j of the TMD clicks. In an actual experiment each coherent state and thus the bin-click probability p_j^{coh} for each bin j is measured multiple thousand times to achieve sufficient statistics. This has to be mimicked in the simulation as well. Therefore, 10^6 coin flips (with outcomes 0 or 1), weighted with the bin probability p_j^{coh} are performed for each bin j for one coherent input state at a time. Next, the array containing zeros and ones, representing a no-click or click in the given bin, is summed along the

bins j . This reveals the total number of clicks that occurred from one incident coherent state, which was split into $N - 1$ sub-pulses corresponding to $N - 1$ bins and lead to N possible outcomes (from zero clicks up to $N - 1$ clicks). Subsequently, a histogram for the N outcomes is calculated based on the numbers of clicks for the 10^6 coin flips. This procedure is repeated for all D coherent input states. The entire process can be reiterated multiple times, each time adding to the already existing histograms for different input states, if 10^6 repetitions are not sufficient. For this simulation the process is repeated four times for a total of 4×10^6 repetitions, to achieve sufficient statistics. By dividing everything by the total number of repetitions, the measurement statistics matrix \mathbf{P} with N columns and D rows can be constructed.

Section 4.1 shows that choosing coherent states with quadratically increasing mean photon numbers $|\alpha_d|^2 = d^2$ with $d \in [0, D - 1]$, where D is the total number of states, is an appropriate method to span the Hilbert space of a detector, as all photon numbers contribute approximately equally. By simulating the matrix \mathbf{P} for ten time bins of the TMD, resulting in $N = 11$ outcomes, it can be seen that the 10-click event is saturated for a mean photon number of $|\alpha_{70}|^2 = 4900$. This is equivalent to a total of $D = 71$ input states and a Hilbert space dimension of $M = 5320$ (chosen according to Section 4.2.1, by including probability amplitudes at six standard deviation greater than the largest coherent state). Note, that the parameters used for the simulation: $\nu = 1.2 \times 10^{-7}$, $R = 0.9137$ and $\eta = 0.8615$, were directly taken from [34]. The photon number distributions of the coherent input states are represented in the coherent input state matrix $\mathbf{F}_{D \times M}$.

Choosing $N = 11$ outcomes with $D = 71$ input states and a Hilbert space dimension of $M = 5320$ leads to a significantly larger POVM matrix $\mathbf{\Pi}$ compared to the 4-pixel SNSPD or the 4-bin spatially multiplexed detector. Therefore, this enables the scalability investigation of the tomographic reconstruction method.

6.2.2 POVM Reconstruction

Based on the matrices \mathbf{P} and \mathbf{F} the POVM matrix $\mathbf{\Pi}$ can be reconstructed following the same procedure as explained in Section 4.2.3. The reconstructed POVM elements π_n based on the simulation of the 10-bin TMD are shown in Fig. 6.2. Already examined properties can be recognized in the POVM elements of the simulation of this device. Firstly, the elements follow a smooth distribution, typical for lossy detectors. Secondly, the POVM element for the largest outcome of this 10-bin TMD π_{10} slowly saturates for larger photon numbers i .

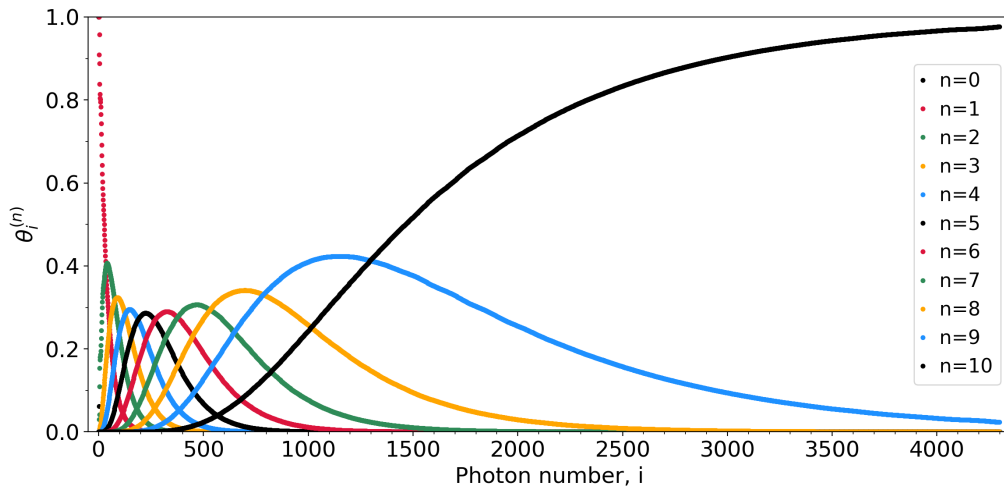


Figure 6.2: Reconstructed POVM elements π_n based on the simulation of the 10-bin time-multiplexed detector shown up to a photon number of $i = 4300$. Note that although the colors in the legend are used more than once, the different outcomes can be easily distinguished, as the distributions shift to the right as n increases.

6.3 Experiment

With the knowledge from the simulation that $D = 71$ input states with quadratically increasing mean photon numbers will saturate a 10-bin time-multiplexed detector, the experiment can be carried out. However, an input state calibration must first be carried out in the same procedure as explained in Chapter 3. This is necessary to calibrate the used attenuations to the mean photon numbers of the coherent states, which characterizes the input states.

6.3.1 Experimental Setup

The experimental setup of the 10-bin TMD varies only slightly from the previous experiments and is shown in Fig. 6.3. The 1556 nm pulsed laser generates coherent states with a repetition rate of 15 kHz, which can be attenuated using the two computer-controlled variable optical attenuators. Before entering the beam splitter loop, which in the experiment is a black-box with an input and an output with fixed coupling constant R and loop efficiency η_{loop} (for more information about the detector design see [34]), the polarization of the input states can be controlled, as this device is strongly polarization dependent. Another polarization controller is placed in front of the SNSPD (the same as in Chapter 3), as the single-photon detector is also polarization dependent. The SNSPD will detect the sub-pulses, created from the beam splitter loop from one impinging pulse with a spacing of $\tau = 156$ ns. A time tagger measures the arrival times of the sub-pulses and stores them

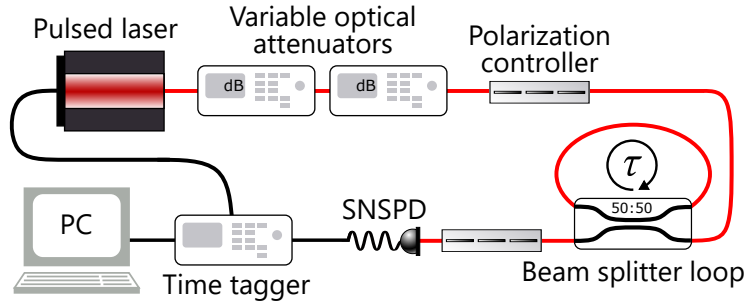


Figure 6.3: Experimental setup for the 10-bin time-multiplexed detector tomography measurement. A 1-pixel SNSPD detects the sub-pulses that are created from one incident coherent state at the beam splitter loop. The pulses are generated from a 1556 nm pulsed laser and can be attenuated by variable optical attenuators. Polarization controllers ensure an optimal polarization, as both the detector and the beam splitter loop are polarization dependent. A time tagger records the detection events in a histogram with ten bins, each separated by the loop length $\tau = 156$ ns.

in a histogram. The histogram, consisting of 1.8×10^5 bins with a width of 10 ps per bin, contains the number of detection events created by the sub-pulses (compare Fig. 6.4). Post processing of this histogram, allows to filter out dark counts or reflections of photons, which can occur especially for large coherent states.

A histogram is measured for each coherent state with a measurement time of 30 s. This corresponds to a total number of 4.5×10^5 pulses due to a laser repetition rate of 15 kHz. Simultaneously, the time tagger measures the repetition rate of the laser (from the laser-synchronization) to account for any laser fluctuations, this way the total number of input pulses for each coherent input state is precisely known. A dark-count measurement (a measurement of the 0-photon inputs state, where all light to the detector is blocked) revealed a dark-count rate of 15 Hz.

The choice of the repetition rate is essential. This is because each input state is split into several sub-pulses, which are spaced according to the loop length τ . However, choosing to record only ten bins, does not mean that the remaining photons inside of the beam splitter loop suddenly disappears. In reality, more than ten sub-pulses are created but only the first ten will be recorded. Therefore, the repetition rate of the laser has to be chosen in a way that an overlap from two subsequent laser pulses in the histogram is not possible. In other words, the photon number inside of the beam splitter loop has to be negligibly small when the next generated laser pulse enters the beam splitter. A repetition rate of 15 kHz corresponds to a spacing of $66 \mu\text{s}$ between subsequent laser pulses. As the histogram records for a time of merely $1.8 \times 10^5 \cdot 10 \text{ ps} = 1.8 \mu\text{s}$, there is no overlap between subsequent laser pulses.

It is worth mentioning that the repetition rate of the laser is limited by the single-photon detector (here a 1-pixel SNSPD) used to detect the states. The reason for this is that the detector can only handle some number of occupied bins per unit time before it latches (for further information see [34]). If the detector enters the latched state, no subsequent photons

can be detected. For this specific device (current biased at $I_{\text{bias}} = 9.0 \mu\text{A}$), latching occurred for repetition rates $> 15 \text{ kHz}$ and mean photon numbers per pulse > 5500 . Fortunately, these limitations still allowed to saturate the 10-bin detector.

6.3.2 Analysis

The recorded histograms for different mean photon numbers contain the information of how many pulses were measured in each of the 1.8×10^5 bins. As already mentioned in the previous section, post processing is used on the histogram to filter out dark counts and reflections, which occur for large mean photon numbers. First of all, the histograms

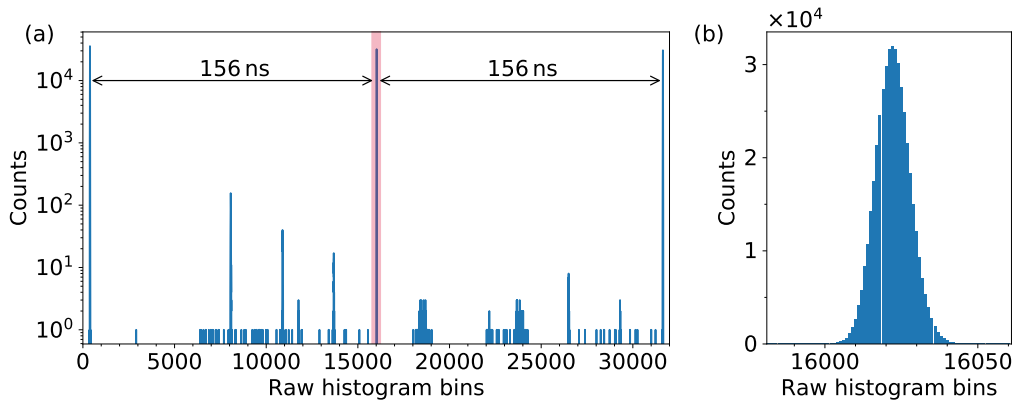


Figure 6.4: (a) Number of counts for the first 3.2×10^4 raw histogram bins for the largest measured coherent state. This corresponds to the first three TMD bins with a spacing of $\tau = 156 \text{ ns}$ or equivalently 15600 raw bins. The logarithmic scale enables the visualization of counts due to dark counts or reflections between the actual TMD bins j . (b) Zooming in on the bin $j = 2$ of the TMD (red shaded region in (a)) reveals a distribution of arrival times of the pulses, determined by the system jitter.

consist of multiple peaks each spaced $\tau = 156 \text{ ns}$ apart, representing the actual time bins j of the TMD (Fig. 6.4(a)). These peaks have a finite width, determined by the system jitter of the components, such as the 1-pixel SNSPD, which is used to detect the impinging pulses (Fig. 6.4(b)). To find the total number of counts in the actual time bins j of the detector, these peaks have to be integrated. The number of raw bins that are integrated determines the noise filtering, hence, as few bins as possible should be integrated to ensure a minimized noise floor. For this measurement a total of 200 raw bins are integrated, which corresponds to a window of 2 ns. With the determined dark-count rate of 15 Hz, the probability to receive a dark count in this window is 3×10^{-8} and therefore negligible.

Afterwards, the probability p_j of a specific bin $j \in [1, 10]$ firing can be calculated as the quotient of the number of counts per bin and the total number of generated laser pulses in the measurement time. The next step is to convert the bin probabilities to click probabilities

to construct the measurement statistics matrix \mathbf{P} , which contains the probability of an n -click event ($n \in [0, 10]$) for each measured coherent input state $|\alpha_d|^2$ with $d \in [0, 70]$.

To calculate the click probabilities p'_n , the counter probability $q_j = 1 - p_j$ of a specific bin j not firing is calculated. Two of the probabilities, the 0-click and 10-click probability are trivial to calculate, as either no bin fired or all bins fired. This corresponds to the product of the counter probabilities q_j or the product of the probabilities p_j for all ten bins, respectively:

$$p'_0 = \prod_{j=1}^{10} q_j, \quad p'_{10} = \prod_{j=1}^{10} p_j. \quad (6.2)$$

The click probabilities for all other events are slightly more complicated to calculate. The process of the calculation for the 1-click probability is used as an example. The necessary one click that constitutes the 1-click probability can occur in any of the ten bins. Therefore, the probabilities that a click occurred in bin $j = 1$ and not in all other bins, that a click occurred in bin $j = 2$ and not in all other bins, that a click occurred in bin $j = 3$ and not in all other bins, etc. have to be added together, which is ultimately described by the expression:

$$p'_1 = \sum_{j=1}^{10} p_j \prod_{\substack{k=1 \\ k \neq j}}^{10} q_k. \quad (6.3)$$

All other n -click probabilities, are calculated following the same procedure: The product of the correct p_j 's and q_j 's have to be summed for all combinations of arranging n ones and $10 - n$ zeros in an array of length 10, where each "1" represents the bin probability p_j corresponding to the placement j of the "1" and each "0" represents the counter probability q_j corresponding to the placement of the "0" in the array of ones and zeros.

The calculation of the click probabilities p'_n is carried out for all $D = 71$ different coherent input states used in the experiment and the measurement statistics matrix \mathbf{P} can be constructed as $P_{d,n} = p'_n|_d$.

The coherent input state matrix \mathbf{F} containing all input states is constructed following the explanation in Section 4.2.1. The fit parameters of the input state calibration that determine the mean photon numbers per pulse \bar{n} as a function of the attenuations α in the experiment are $b = 4.029^{+0.025}_{-0.027}$ for the y-axis intercept and $m = -0.09937 \pm 0.00022$ for the slope of the linear fit.

The last step to get access to the POVM elements π_n of the 10-bin TMD is to reconstruct the matrix $\mathbf{\Pi}$ based on the previously constructed measurement statistics matrix \mathbf{P} and the coherent input state matrix \mathbf{F} . The general procedure of the reconstruction is explained in Section 4.2.3 for the 4-pixel SNSPD and also applies to this detector.

6.3.3 Results

The reconstructed POVM elements π_n of the 10-bin TMD are shown in Fig. 6.5. In general the individual distributions behave as expected, as they show smoothness and a close resemblance to the reconstructed POVM elements based on the simulation from Fig. 6.2. These results show that the tomographic reconstruction method reveals physically sensible knowledge and proves the applicability of the method to larger detector arrays.

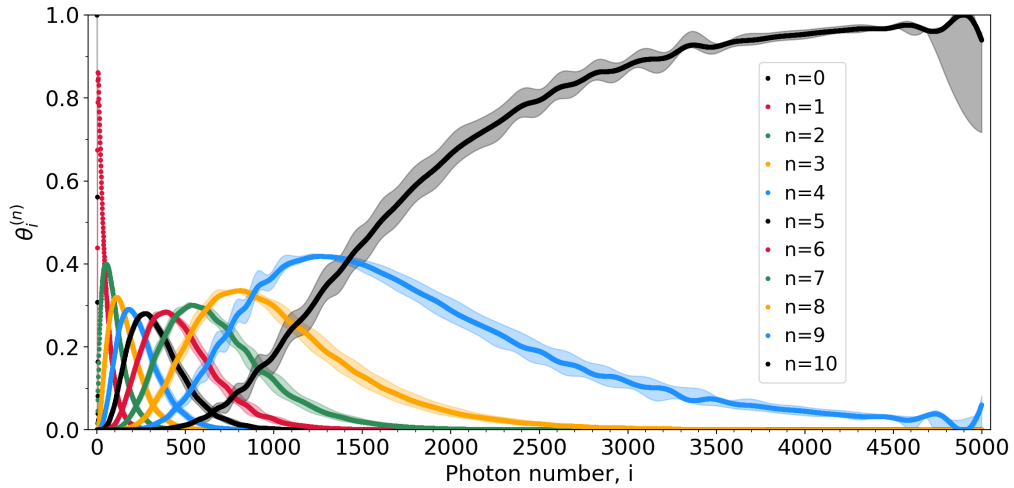


Figure 6.5: Reconstructed POVM elements π_n of the 10-bin time-multiplexed detector. Errors are based on assuming 5% uncertainty on the efficiency of the calibration detector. Although, colors in the legend are used more than once, the different outcomes can be easily distinguished, as the distributions shift to the right as n increases. The trend of the distributions for photon numbers $i > 4900$ stems from a lack of information in the input state matrix F and is explained in Section 4.3.6.

The oscillations in the distributions in Fig. 6.5 can be attributed to insufficient statistics, as these oscillations could also be observed for POVM elements based on simulations with less repetitions. This means, the 30 s measurement time per coherent input state (compare Section 6.3.1) was chosen be slightly too low. Therefore, a longer measurement time of one minute, to achieve almost 10^6 total pulses, has to be considered for further improvements of the experiment. However, when investigating significantly more bins of the time-multiplexed detector, where more and larger coherent states are necessary, the duration of each measurement should be carefully chosen so ensure sufficient statistics and not too long experiments, to reduce for example the effects of temporal laser fluctuations, which would increase the uncertainty in the input states.

Calculating the efficiency with the definition from Eq. (4.7) reveals an efficiency of $\eta = (44 \pm 3) \%$ for 10-bin TMD. Although, the SNSPD used for the detection of the pulses has an efficiency of 83%, the lower efficiency of the TMD stems from extra loss inside the beam

splitter loop (determined by the loop efficiency η_{loop}). The lower efficiency, compared to the 4-pixel and 4-bin detector, in combination with the probabilistic out-coupling of photons by the beam splitter leads to a small Purity (π_n) for all outcomes (green bars in Fig. 7.1). The small purity, which corresponds to a poor photon-number resolving performance, as many orthogonal input states lead to the same outcome n , is by design. This is because the time-multiplexed loop-detector is build to have a high dynamic range for measuring single photons and bright light [34].

The 4-bin spatially multiplexed detector (compare the cross-talk analysis in Section 5.3) was employed to give insight about the cross-talk probability definition from Section 4.3.4. However, the results did not fully match the expectations, as an elevated $p(2|1)$ probability was observed, which leads to the existence of cross-talk between the separate detectors. Although, this result has to be observed in more detail with further experiments, the 10-bin time-multiplexed detector can also give more insight about cross-talk. This detector design relies on temporal bins for the separation of different outcomes and consists of only one single-photon detector. Hence, no cross-talk should be observed, since there is no second detector, that may click as a result to a first detector firing. Using Eq. (4.11) with the probabilities $p(2|1) = (4.6 \pm 2.8) \times 10^{-6}$, $p(1|1) = 0.44 \pm 0.03$ and $p(1|0) = p_{\text{dark}} = (0.0 \pm 4.1) \times 10^{-7}$ from the reconstruction, the cross-talk probability of the 10-bin detector can be estimated by $p_{\text{xtalk}} = (4.6 \pm 2.8) \times 10^{-4} \%$, which is negligibly small. Nevertheless, just like the 4-bin detector, this will also benefit from further investigations utilizing coherent states with a smaller uncertainty in their mean photon numbers, leading to a more accurate reconstruction. Additionally, these results are based on not perfectly sufficient statistics, which has to be considered as an improvement for further experiments.

Important to note is that the reconstruction predicts a dark-count probability of the device of $p_{\text{dark}} = 0$ for the main and the lower error reconstruction, however, a probability of 4.1×10^{-7} for the upper error. This may indicate a limit to the accuracy of the reconstruction process. The expected dark-count probability per pulse and per 2 ns bin was merely 3×10^{-8} (compare Section 6.3.2). It is possible that the reconstruction is not able to accurately describe these small numbers. This observation can be supported by the occurrence of contributions $\theta_0^{(n \geq 1)}$ in the POVM matrix $\mathbf{\Pi}$ in the order of 10^{-8} (Fig. 6.6). With a measured dark-count probability of 3×10^{-8} per bin, the probability $p(2|0) = \theta_0^{(2)}$, corresponding to two clicks given no incident photons or equivalently two dark-count photons, should already be in the order of 10^{-16} . Higher click events based on merely dark-counts should not be observed in the experiment as they are exceptionally unlikely. The fact, that the POVM matrix $\mathbf{\Pi}$ shows contributions for higher click events for the 0-photon input state in the same order of magnitude (Fig. 6.6), leads to the assumption that the accuracy of the reconstruction may indeed be in the order of 10^{-7} .

The reconstruction of the POVM elements of the 10-bin TMD took roughly 20 minutes under full load of the computer. This does not fit the linear dependency observed in Section 4.3.6. In fact, the linear fit (compare Fig. A.2) would predict a calculation time of $y = -0.11395 + 0.00355 \cdot (5328 \cdot 11) \approx 208$ s, where $M = 5328$ and $N = 11$ are the size of the matrix $\mathbf{\Pi}$. The six times slower reconstruction time can partially be attributed to the

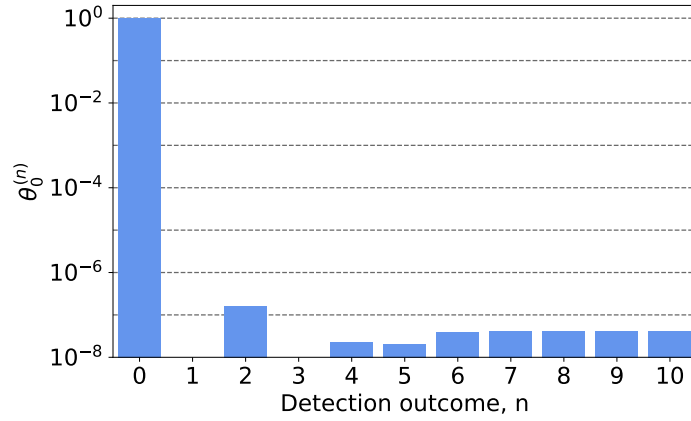


Figure 6.6: POVM elements $\theta_0^{(n)}$, corresponding to the first row of the POVM matrix $\mathbf{\Pi}$ of the 10-bin TMD on a logarithmic scale. The elements $\theta_0^{(1)} = \theta_0^{(3)} = 0$. The contributions in the order of 10^{-8} may indicate a limit in the accuracy of the tomographic reconstruction.

smoothing function $g(\mathbf{\Pi})$. It takes already more than 50 s to calculate the expression from Eq. (2.15), which consists of $N \cdot (M - 1)$ summands of elements from the matrix $\mathbf{\Pi}$, which is a *CVXPY*-variable. Reconstructing the POVM elements without the smoothing function $g(\mathbf{\Pi})$ takes only roughly 100 s and the optimization problem from Eq. (2.16) is minimized with fewer iterations and less time per iteration. This means, when smoothing is applied and some matrix size of $\mathbf{\Pi}_{M \times N}$ is exceeded, the reconstruction time deviates from the linear dependency (observed for small matrix sizes) and follows a different nonlinear trend. These observations place a limit on the physical size of the detector arrays that can be investigated using this method, at least when using a standard desktop computer.

Conclusion and Outlook

7

In this thesis quantum detector tomography was applied to several single-photon detector designs, in order to investigate the tomographic reconstruction as a characterization method. The positive operator valued measures (POVMs) fully describe a device without recourse to the underlying working principle or type of the detector. Quantum detector tomography enables the determination of several figures of merit by conducting merely one well-designed experiment in combination with a tomographic reconstruction of the POVM matrix $\mathbf{\Pi}$. These are advantages over alternative characterization methods, such as model-based techniques or an individual determination of the figures of merit, as these are based on prior knowledge about the detector or multiple experiments, respectively.

Chapter 4 introduces definitions for the efficiency η , dark-count probability p_{dark} and cross-talk probability p_{xtalk} merely based on four POVM matrix elements, namely the probabilities $p(0|1)$, $p(1|0)$, $p(1|1)$ and $p(2|1)$. Comparing the results from these definitions with an individual determination of the efficiency and dark-count probability of the 4-pixel SNSPD reveals a good agreement. Hence, the established definitions are valid, which additionally confirms the advantage of quantum detector tomography of characterizing multiple figures of merit at once.

Investigating the Purity (π_n) and correspondingly the effective Hilbert space dimension $M_{\text{eff}}(n)$ for the different POVM elements π_n confirms that all three detectors (4-pixel SNSPD array, 4-bin spatially multiplexed and 10-bin time-multiplexed) are not inherently photon-number resolving, which stems from the fact that they are based on click-detectors and is shown in the POVM matrix $\mathbf{\Pi}$ by significant contributions from multiple orthogonal input states to the same detection outcomes n . A comparison between the purities for the detectors (Fig. 7.1) reveals that the 4-pixel and the 4-bin device can almost be used interchangeably, as they also show similar efficiencies and dark-count probabilities. Since these two detectors are limited to $N = 5$ outcomes, the time-multiplexed detector design with a variable number of outcomes is the choice for experiments that require more outcomes. However, the TMD has poor purities, which stems from the fact that it is designed to have a high dynamic range [34].

Regarding the purity, it would be interesting to apply the tomographic reconstruction method to photon-number resolving detectors such as transition edge sensors, which should reveal purities close to unity due to their inherent single-photon energy resolution.

The results from the tomographic reconstructions of the three different detector designs, regarding the cross-talk probability, do not perfectly agree with the expectations, as the latter two detectors show a non-zero p_{xtalk} . Nevertheless, the results are physically relevant

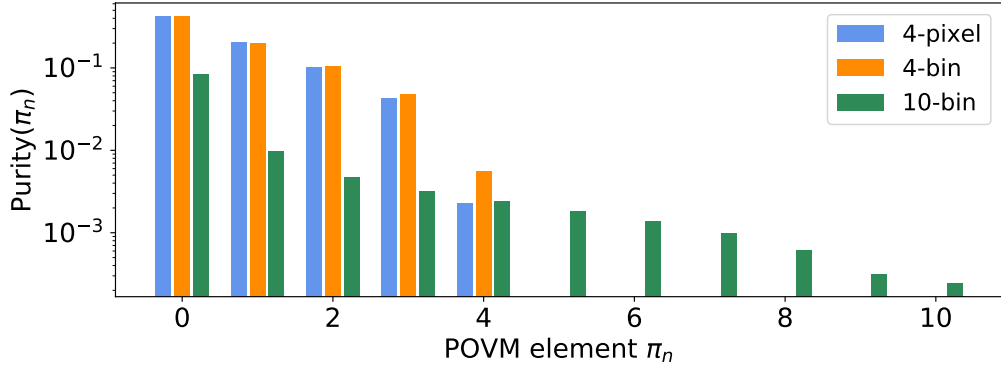


Figure 7.1: Comparison of the Purity(π_n) for the investigated detectors: 4-pixel SNSPD (blue), 4-bin spatially multiplexed detector (orange) and 10-bin TMD (green). Note that the Purity(π_4) from the 4-bin detector is larger compared to the 4-pixel detector. This stems from the smaller Hilbert space dimension for the 4-bin detector, therefore, the purities for π_4 cannot be compared directly.

and a pattern can be observed. The 4-pixel device was expected to definitely show cross-talk, as the individual pixels are wired in series and current density fluctuations in combination with a high bias current I_{bias} will inevitably lead to cross-talk. This was confirmed by the large probability $p_{\text{xtalk}}^{(4\text{-pixel})} = (14 \pm 1) \%$.

The 4-bin spatially multiplexed detector should in principle not be effected by cross-talk, as four separate single-photon detectors are used for the experiment, each current biased and read out individually. Although, a connection between the devices does almost certainly not exist (compare Section 5.3), it may still be possible that the non-zero cross-talk probability $p_{\text{xtalk}}^{(4\text{-bin})} = (3.6 \pm 0.1) \%$ can be explained by the fact that multiple devices are used in this design.

Lastly, the 10-bin TMD, which utilizes only one SNSPD to detect the input states, is the device least expected to show cross-talk. This is confirmed by the negligibly small probability $p_{\text{xtalk}}^{(10\text{-bin})} = (4.6 \pm 2.8) \times 10^{-4} \%$. These results show that the cross-talk definition from Eq. (4.11) is valid, however, further investigations are necessary to confirm the inconsistency in the non-zero probabilities for the 4-bin and the 10-bin detector. Utilizing a more accurate detector, which has a smaller uncertainty in the efficiency, to calibrate the input states will be beneficial, as its leads to smaller uncertainties in the reconstructed POVM elements. Using single-photon Fock states to individually investigate the cross-talk phenomenon would lead to a deeper understanding of the the different detectors. Single-photon Fock states in combination with very small coincidence windows, to limit the dark-count probability per pulse even further, will reveal cross-talk between detectors by an elevated 2-click count rate.

The investigations from Chapter 6 suggest that the tomographic reconstruction method used in this thesis is limited to a certain detector array size. When utilizing a standard desktop computer, the full reconstruction of large POVM matrices $\mathbf{\Pi}$ will eventually be too demanding, partially due to the smoothing function $g(\mathbf{\Pi})$. Including coherent states with very large mean photon numbers can at some point also lead to challenges in the calculation of the input state matrix \mathbf{F} , as the calculation of large factorials can be demanding. For large mean photon numbers Stirling's formula can be used to transform the Poisson distribution into a Gaussian distribution. These serve as excellent approximations and can be calculated more efficiently.

When only interested in the main figures of merit: efficiency, dark-count probability and cross-talk probability, Section 4.3.6 has shown that it is certainly possible to execute a "truncated reconstruction", without spanning the entire Hilbert space of the detector under test, and still determine the figures of merit with a good accuracy (indicated by small relative deviations $\delta\theta_i^{(n)}$ and a near unity fidelity of $\mathcal{F} \geq 99.8\%$). This can enable the characterization of large detector arrays that would otherwise exceed the limitations of this method.

The next interesting step would be, to apply the tomographic reconstruction method to larger spatial arrays of SNSPDs. An 8×8 SNSPD array with row-column readout [18], which has nine outcomes (depending on the definition) should still be a suitable candidate for a full reconstruction of the POVM elements.

-
- [1] F. Arute, K. Arya, R. Babbush, D. Bacon, J. C. Bardin, R. Barends, R. Biswas, S. Boixo, F. G. S. L. Brandao, D. A. Buell, et al., Quantum supremacy using a programmable superconducting processor, *Nature* **574**, 505 (2019).
- [2] I. A. Walmsley, Quantum optics: Science and technology in a new light, *Science* **348**, 525 (2015).
- [3] Y. Mao, B.-X. Wang, C. Zhao, G. Wang, R. Wang, H. Wang, F. Zhou, J. Nie, Q. Chen, Y. Zhao, et al., Integrating quantum key distribution with classical communications in backbone fiber network, *Optics Express* **26**, 6010 (2018).
- [4] F. Flamini, N. Spagnolo, and F. Sciarrino, Photonic quantum information processing: a review, *Reports on Progress in Physics* **82**, 16001 (2018).
- [5] G. N. Gol'Tsman, O. Okunev, G. Chulkova, A. Lipatov, A. Semenov, K. Smirnov, B. Voronov, A. Dzardanov, C. Williams, and R. Sobolewski, Picosecond superconducting single-photon optical detector, *Applied Physics Letters* **79**, 705 (2001).
- [6] C. M. Natarajan, M. G. Tanner, and R. H. Hadfield, Superconducting nanowire single-photon detectors: physics and applications, *Superconductor Science and Technology* **25**, 63001 (2012).
- [7] F. Marsili, V. B. Verma, J. A. Stern, S. Harrington, A. E. Lita, T. Gerrits, I. Vayshenker, B. Baek, M. D. Shaw, R. P. Mirin, et al., Detecting single infrared photons with 93% system efficiency, *Nature Photonics* **7**, 210 (2013).
- [8] H. Shibata, K. Shimizu, H. Takesue, and Y. Tokura, Ultimate low system dark-count rate for superconducting nanowire single-photon detector, *Optics Letters* **40**, 3428 (2015).
- [9] I. Esmail Zadeh, J. W. N. Los, R. B. M. Gourgues, V. Steinmetz, G. Bulgarini, S. M. Dobrovolskiy, V. Zwiller, and S. N. Dorenbos, Single-photon detectors combining high efficiency, high detection rates, and ultra-high timing resolution, *Apl Photonics* **2**, 111301 (2017).
- [10] B. Korzh, Q.-Y. Zhao, J. P. Allmaras, S. Frasca, T. M. Autry, E. A. Bersin, A. D. Beyer, R. M. Briggs, B. Bumble, M. Colangelo, et al., Demonstration of sub-3 ps temporal

- resolution with a superconducting nanowire single-photon detector, *Nature Photonics* **14**, 250 (2020).
- [11] E. A. Dauler, B. S. Robinson, A. J. Kerman, J. K. W. Yang, K. M. Rosfjord, V. Anant, B. Voronov, G. Gol'tsman, and K. K. Berggren, Multi-element superconducting nanowire single-photon detector, *IEEE Transactions on Applied Superconductivity* **17**, 279 (2007).
- [12] A. Divochiy, F. Marsili, D. Bitauld, A. Gaggero, R. Leoni, F. Mattioli, A. Korneev, V. Seleznev, N. Kaurova, O. Minaeva, et al., Superconducting nanowire photon-number-resolving detector at telecommunication wavelengths, *Nature Photonics* **2**, 302 (2008).
- [13] F. Marsili, D. Bitauld, A. Gaggero, S. Jahanmirinejad, R. Leoni, F. Mattioli, and A. Fiore, Physics and application of photon number resolving detectors based on superconducting parallel nanowires, *New Journal of Physics* **11**, 45022 (2009).
- [14] S. Jahanmirinejad, G. Frucci, F. Mattioli, D. Sahin, A. Gaggero, R. Leoni, and A. Fiore, Photon-number resolving detector based on a series array of superconducting nanowires, *Applied Physics Letters* **101**, 72602 (2012).
- [15] Q. Zhao, A. McCaughan, F. Bellei, F. Najafi, D. De Fazio, A. Dane, Y. Ivry, and K. K. Berggren, Superconducting-nanowire single-photon-detector linear array, *Applied Physics Letters* **103**, 142602 (2013).
- [16] D. Rosenberg, A. J. Kerman, R. J. Molnar, and E. A. Dauler, High-speed and high-efficiency superconducting nanowire single photon detector array, *Optics Express* **21**, 1440 (2013).
- [17] V. B. Verma, R. Horansky, F. Marsili, J. A. Stern, M. D. Shaw, A. E. Lita, R. P. Mirin, and S. W. Nam, A four-pixel single-photon pulse-position array fabricated from WSi superconducting nanowire single-photon detectors, *Applied Physics Letters* **104**, 51115 (2014).
- [18] M. S. Allman, V. B. Verma, M. Stevens, T. Gerrits, R. D. Horansky, A. E. Lita, F. Marsili, A. Beyer, M. D. Shaw, D. Kumor, et al., A near-infrared 64-pixel superconducting nanowire single photon detector array with integrated multiplexed readout, *Applied Physics Letters* **106**, 192601 (2015).
- [19] F. Najafi, J. Mower, N. C. Harris, F. Bellei, A. Dane, C. Lee, X. Hu, P. Kharel, F. Marsili, S. Assefa, et al., On-chip detection of non-classical light by scalable integration of single-photon detectors, *Nature Communications* **6**, 1 (2015).
- [20] Q. Chen, B. Zhang, L. Zhang, R. Ge, R. Xu, Y. Wu, X. Tu, X. Jia, L. Kang, J. Chen, et al., A 16-pixel NBN nanowire single photon detector coupled with 300 micrometer fiber, *arXiv preprint arXiv:1811.09779* (2018).

-
- [21] X. Tao, S. Chen, Y. Chen, L. Wang, X. Li, X. Tu, X. Jia, Q. Zhao, L. Zhang, L. Kang, et al., A high speed and high efficiency superconducting photon number resolving detector, *Superconductor Science and Technology* **32**, 64002 (2019).
- [22] E. E. Wollman, V. B. Verma, A. E. Lita, W. H. Farr, M. D. Shaw, R. P. Mirin, and S. W. Nam, Kilopixel array of superconducting nanowire single-photon detectors, *Optics Express* **27**, 35279 (2019).
- [23] A. N. McCaughan, Readout architectures for superconducting nanowire single photon detectors, *Superconductor Science and Technology* **31** (2018).
- [24] S. Miyajima, M. Yabuno, S. Miki, T. Yamashita, and H. Terai, High-time-resolved 64-channel single-flux quantum-based address encoder integrated with a multi-pixel superconducting nanowire single-photon detector, *Optics Express* **26**, 29045 (2018).
- [25] C. Cahall, D. J. Gauthier, and J. Kim, Scalable cryogenic readout circuit for a superconducting nanowire single-photon detector system, *Review of Scientific Instruments* **89**, 63117 (2018).
- [26] A. Gaggero, F. Martini, F. Mattioli, F. Chiarello, R. Cernansky, A. Politi, and R. Leoni, Amplitude-multiplexed readout of single photon detectors based on superconducting nanowires, *Optica* **6**, 823 (2019).
- [27] J. Tiedau, T. Schapeler, V. Anant, H. Fedder, C. Silberhorn, and T. J. Bartley, Single-channel electronic readout of a multipixel superconducting nanowire single photon detector, *Optics Express* **28**, 5528 (2020).
- [28] J. P. Allmaras, E. E. Wollman, A. D. Beyer, R. M. Briggs, B. A. Korzh, B. Bumble, and M. D. Shaw, Demonstration of a Thermally Coupled Row-Column SNSPD Imaging Array, *Nano Letters* **20**, 2163 (2020).
- [29] N. Takeuchi, F. China, S. Miki, S. Miyajima, M. Yabuno, N. Yoshikawa, and H. Terai, Scalable readout interface for superconducting nanowire single-photon detectors using AQFP and RSFQ logic families, *Optics Express* **28**, 15824 (2020).
- [30] C. Cahall, K. L. Nicolich, N. T. Islam, G. P. Lafyatis, A. J. Miller, D. J. Gauthier, and J. Kim, Multi-photon detection using a conventional superconducting nanowire single-photon detector, *Optica* **4**, 1534 (2017).
- [31] D. Zhu, Q.-Y. Zhao, H. Choi, T.-J. Lu, A. E. Dane, D. Englund, and K. K. Berggren, A scalable multi-photon coincidence detector based on superconducting nanowires, *Nature Nanotechnology* **13**, 596 (2018).

- [32] D. Zhu, M. Colangelo, C. Chen, B. A. Korzh, F. N. C. Wong, M. D. Shaw, and K. K. Berggren, Resolving Photon Numbers Using a Superconducting Nanowire with Impedance-Matching Taper, *Nano Letters* **20**, 3858 (2020).
- [33] C. M. Natarajan, L. Zhang, H. Coldenstrodt-Ronge, G. Donati, S. N. Dorenbos, V. Zwiller, I. A. Walmsley, and R. H. Hadfield, Quantum detector tomography of a time-multiplexed superconducting nanowire single-photon detector at telecom wavelengths, *Optics Express* **21**, 893 (2013).
- [34] J. Tiedau, E. Meyer-Scott, T. Nitsche, S. Barkhofen, T. J. Bartley, and C. Silberhorn, A high dynamic range optical detector for measuring single photons and bright light, *Optics Express* **27**, 1 (2019).
- [35] S. Miki, T. Yamashita, Z. Wang, and H. Terai, A 64-pixel NbTiN superconducting nanowire single-photon detector array for spatially resolved photon detection, *Optics Express* **22**, 7811 (2014).
- [36] P.-A. Moreau, E. Toninelli, T. Gregory, and M. J. Padgett, Imaging with quantum states of light, *Nature Reviews Physics* **1**, 367 (2019).
- [37] M. D. Shaw, F. Marsili, A. D. Beyer, J. A. Stern, G. V. Resta, P. Ravindran, S. Chang, J. Bardin, D. S. Russell, J. W. Gin, et al., “Arrays of WSi superconducting nanowire single photon detectors for deep-space optical communications”, in 2015 conference on lasers and electro-optics (cleo) (IEEE, 2015), p. 1.
- [38] Y. Hochberg, I. Charaev, S.-W. Nam, V. Verma, M. Colangelo, and K. K. Berggren, Detecting sub-GeV dark matter with superconducting nanowires, *Physical Review Letters* **123**, 151802 (2019).
- [39] A. Migdall, S. V. Polyakov, J. Fan, and J. C. Bienfang, *Single-Photon Generation and Detection: Physics and Applications*, ISSN (Elsevier Science, 2013).
- [40] J. S. Lundeen, A. Feito, H. Coldenstrodt-Ronge, K. L. Pregnell, C. Silberhorn, T. C. Ralph, J. Eisert, M. B. Plenio, and I. A. Walmsley, Tomography of quantum detectors, *Nature Physics* **5**, 27 (2009).
- [41] A. Feito, J. S. Lundeen, H. Coldenstrodt-Ronge, J. Eisert, M. B. Plenio, and I. A. Walmsley, Measuring measurement: theory and practice, *New Journal of Physics* **11**, 93038 (2009).
- [42] F. Piacentini, M. P. Levi, A. Avella, M. López, S. Kück, S. V. Polyakov, I. P. Degiovanni, G. Brida, and M. Genovese, Positive operator-valued measure reconstruction of a beam-splitter tree-based photon-number-resolving detector, *Optics Letters* **40**, 1548 (2015).

-
- [43] P. C. Humphreys, B. J. Metcalf, T. Gerrits, T. Hiemstra, A. E. Lita, J. Nunn, S. W. Nam, A. Datta, W. S. Kolthammer, and I. A. Walmsley, Tomography of photon-number resolving continuous-output detectors, *New Journal of Physics* **17**, 103044 (2015).
- [44] L. Zhang, H. B. Coldenstrodt-Ronge, A. Datta, G. Puentes, J. S. Lundeen, X.-M. Jin, B. J. Smith, M. B. Plenio, and I. A. Walmsley, Mapping coherence in measurement via full quantum tomography of a hybrid optical detector, *Nature Photonics* **6**, 364 (2012).
- [45] M. Cooper, M. Karpiński, and B. J. Smith, Local mapping of detector response for reliable quantum state estimation, *Nature Communications* **5**, 4332 (2014).
- [46] P. Eraerds, M. Legré, A. Rochas, H. Zbinden, and N. Gisin, SiPM for fast photon-counting and multiphoton detection, *Optics Express* **15**, 14539 (2007).
- [47] M. Akiba, K. Tsujino, K. Sato, and M. Sasaki, A multipixel silicon APD with ultralow dark count rate at liquid nitrogen temperature, arXiv preprint arXiv:0812.0634 (2008).
- [48] I. Afek, A. Natan, O. Ambar, and Y. Silberberg, Quantum state measurements using multipixel photon detectors, *Physical Review A* **79**, 43830 (2009).
- [49] M. Ramilli, A. Allevi, V. Chmilla, M. Bondani, M. Caccia, and A. Andreoni, Photon-number statistics with silicon photomultipliers, *Journal of the Optical Society of America B* **27**, 852 (2010).
- [50] D. A. Kalashnikov, S. H. Tan, M. V. Chekhova, and L. A. Krivitsky, Accessing photon bunching with a photon number resolving multi-pixel detector, *Optics Express* **19**, 9352 (2011).
- [51] D. A. Kalashnikov, S.-H. Tan, and L. A. Krivitsky, Crosstalk calibration of multi-pixel photon counters using coherent states, *Optics Express* **20**, 5044 (2012).
- [52] L. Dovrat, M. Bakstein, D. Istrati, A. Shaham, and H. S. Eisenberg, Measurements of the dependence of the photon-number distribution on the number of modes in parametric down-conversion, *Optics Express* **20**, 2266 (2012).
- [53] R. Nehra, C.-H. Chang, Q. Yu, A. Beling, and O. Pfister, Photon-number-resolving segmented detectors based on single-photon avalanche-photodiodes, *Optics Express* **28**, 3660 (2020).
- [54] V. B. Verma, B. Korzh, F. Bussières, R. D. Horansky, S. D. Dyer, A. E. Lita, I. Vayshenker, F. Marsili, M. D. Shaw, H. Zbinden, et al., High-efficiency superconducting nanowire single-photon detectors fabricated from MoSi thin-films, *Optics Express* **23**, 33792 (2015).

- [55] J. K. W. Yang, A. J. Kerman, E. A. Dauler, V. Anant, K. M. Rosfjord, and K. K. Berggren, Modeling the electrical and thermal response of superconducting nanowire single-photon detectors, *IEEE Transactions on Applied Superconductivity* **17**, 581 (2007).
- [56] D. V. Reddy, A. E. Lita, S. W. Nam, R. P. Mirin, and V. B. Verma, “Achieving 98% system efficiency at 1550 nm in superconducting nanowire single photon detectors”, in Conference on coherence and quantum optics (Optical Society of America, 2019), W2B–2.
- [57] J. P. Höpker, M. Bartnick, E. Meyer-Scott, F. Thiele, S. Krapick, N. Montaut, M. Santandrea, H. Herrmann, S. Lengeling, R. Ricken, et al., “Towards integrated superconducting detectors on lithium niobate waveguides”, in Quantum photonic devices, Vol. 10358 (International Society for Optics and Photonics, 2017), p. 1035809.
- [58] M. A. Nielsen and I. L. Chuang, *Quantum Computation and Quantum Information: 10th Anniversary Edition* (Cambridge University Press, 2010).
- [59] C. Gerry, P. Knight, and P. L. Knight, *Introductory quantum optics* (Cambridge university press, 2005).
- [60] G. H. Golub and C. F. Van Loan, *Matrix Computations*, Johns Hopkins Studies in the Mathematical Sciences (Johns Hopkins University Press, 2013).
- [61] S. J. van Enk, Photodetector figures of merit in terms of POVMs, *Journal of Physics Communications* **1**, 45001 (2017).
- [62] M. Fox, *Quantum optics: an introduction*, Vol. 15 (OUP Oxford, 2006).
- [63] *Swabian Instruments Time Tagger User Manual*, 2.6.6.14 (Swabian Instruments, 2020).
- [64] N. M. Montaut, “Integrated Single Photon Sources: Development to Benchmarking”, PhD thesis (Universitätsbibliothek, 2019).
- [65] T. Schapeler, J. P. Hoepker, and T. J. Bartley, Quantum detector tomography of a 2x2 multi-pixel array of superconducting nanowire single photon detectors, arXiv preprint arXiv:2007.16048 (2020).
- [66] S. Diamond and S. Boyd, CVXPY: A Python-Embedded Modeling Language for Convex Optimization, *Journal of Machine Learning Research* **17**, 1 (2016).
- [67] A. Agrawal, R. Verschueren, S. Diamond, and S. Boyd, A Rewriting System for Convex Optimization Problems, *Journal of Control and Decision* **5**, 42 (2018).

Appendix

A

Formulas for the Second-Order Correlation Function

This section contains, as an addition to Section 3.3, detailed formulas and calculations for the overall $g^{(2)}(0)$ -value of the laser used in this thesis. First, the second-order correlation function at $\tau = 0$ for all coherent input states $|\alpha_d\rangle^2$ with $d \in [0, 70]$ and all combinations of two detectors $XY \in \{AB, AC, AD, BC, BD, CD\}$ is calculated

$$g_{XY}^{(2)}(0)|_d = \frac{c_{XY}|_d \cdot c_0|_d}{c_X|_d \cdot c_Y|_d}, \quad (\text{A.1})$$

where the corresponding errors $\Delta g_{XY}^{(2)}(0)|_d$ are calculated according to the Gaussian error propagation. Afterwards, the weighted mean between all input states is calculated for each combination of two detectors, according to the formula

$$\overline{g_{XY}^{(2)}(0)} = \frac{\sum_d w_{XY}|_d \cdot g_{XY}^{(2)}(0)|_d}{\sum_d w_{XY}|_d} \quad (\text{A.2})$$

with the weights

$$w_{XY}|_d = \frac{1}{\left(\Delta g_{XY}^{(2)}(0)|_d\right)^2}. \quad (\text{A.3})$$

The uncertainty of the weighted mean is given by the standard error of the weighted mean

$$\overline{\Delta g_{XY}^{(2)}(0)} = \sqrt{\frac{1}{\sum_d w_{XY}|_d}}. \quad (\text{A.4})$$

Finally, the mean value of the weighted means is calculated according to

$$g^{(2)}(0) = \frac{1}{6} \left(\overline{g_{AB}^{(2)}(0)} + \overline{g_{AC}^{(2)}(0)} + \overline{g_{AD}^{(2)}(0)} + \overline{g_{BC}^{(2)}(0)} + \overline{g_{BD}^{(2)}(0)} + \overline{g_{CD}^{(2)}(0)} \right), \quad (\text{A.5})$$

where the error of this measure is determined using Gaussian error propagation based on the standard error of the weighted means.

Tables

Table A.1: This table shows the used attenuations α in decibel and the resulting mean photon numbers per pulse \bar{n} , which can be calculated using Eq. (3.4), for the 4-pixel SNSPD detector tomography experiment. The last entry for the attenuation labeled “inf” corresponds to the case, where the entire input light is blocked for the dark-count measurement.

α [dB]	\bar{n}	α [dB]	\bar{n}
19.0	332.591	26.2	64.9911
19.6	290.283	27.4	49.5083
20.2	253.358	28.8	36.0418
20.8	221.129	30.4	25.0748
21.4	193	32.4	15.9323
22.0	168.45	34.8	9.24541
22.6	147.022	38.4	4.08694
23.4	122.63	41.4	1.00189
24.2	102.285	inf	0
25.2	81.5331		

Table A.2: This table shows the reconstructed POVM elements π_n of the 4-pixel SNSPD shown up to a photon number of $i = 10$.

	π_0	π_1	π_2	π_3	π_4
$ 0\rangle\langle 0 $	0.999993	7.67×10^{-6}	1.53×10^{-7}	0	3.32×10^{-7}
$ 1\rangle\langle 1 $	0.372409	0.489448	0.138144	0	0
$ 2\rangle\langle 2 $	0.128746	0.516624	0.298308	0.0515508	0.00477576
$ 3\rangle\langle 3 $	0.0502706	0.344045	0.408563	0.175905	0.0212215
$ 4\rangle\langle 4 $	0.0222354	0.176156	0.450918	0.294802	0.0558914
$ 5\rangle\langle 5 $	0.00627289	0.0771496	0.427134	0.380631	0.108811
$ 6\rangle\langle 6 $	1.56×10^{-5}	0.0379913	0.355766	0.431488	0.174729
$ 7\rangle\langle 7 $	1.32×10^{-5}	0.0299692	0.264699	0.456245	0.249068
$ 8\rangle\langle 8 $	9.36×10^{-6}	0.0282436	0.179195	0.464382	0.328171
$ 9\rangle\langle 9 $	1.14×10^{-5}	0.0193963	0.11332	0.460311	0.406961
$ 10\rangle\langle 10 $	1.86×10^{-5}	0.00510006	0.0701857	0.444678	0.480014

Table A.3: This table contains the information about the correct bias current, voltage threshold for the readout with the time tagger and artificial deadtime (set in the time tagger) for all detectors used in this thesis.

Name	Type	I_{bias} [μA]	Threshold [mV]	Dead time [ns]
L225	1-pixel SNSPD	9.2	50	60
L254	1-pixel SNSPD	11	20	60
S303	1-pixel SNSPD	5.8	50	60
L285	4-pixel SNSPD	17	17 (1-click event)	150

Table A.4: This table shows the used attenuations α in decibel and the resulting mean photon numbers per pulse \bar{n} , which can be calculated using Eq. (3.4), for the 4-bin spatially multiplexed detector tomography experiment. The last entry for the attenuation labeled “inf” corresponds to the case, where the entire input light is blocked for the dark-count measurement.

α [dB]	\bar{n}
23.2	122.147
24.0	101.98
25.0	81.2251
26.0	64.7515
27.2	49.3312
28.6	35.9175
30.2	24.9921
32.0	16.6192
34.6	9.21862
38.2	4.00765
44.2	0.99989
inf	0

Figures

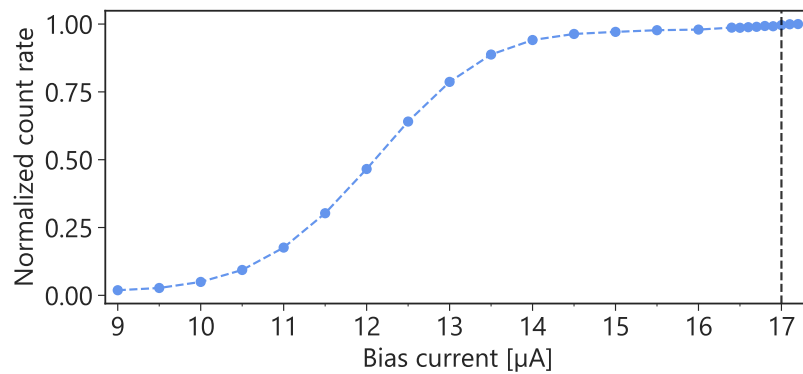


Figure A.1: Bias saturation curve for the “at least 1-click” event of the 4-pixel SNSPD. The normalized count rate is plotted against the bias current, which clearly shows a bias plateau. From this, in combination with the “threshold sweep”, the bias current is chosen to be 17 μA (marked by the black vertical dashed line).

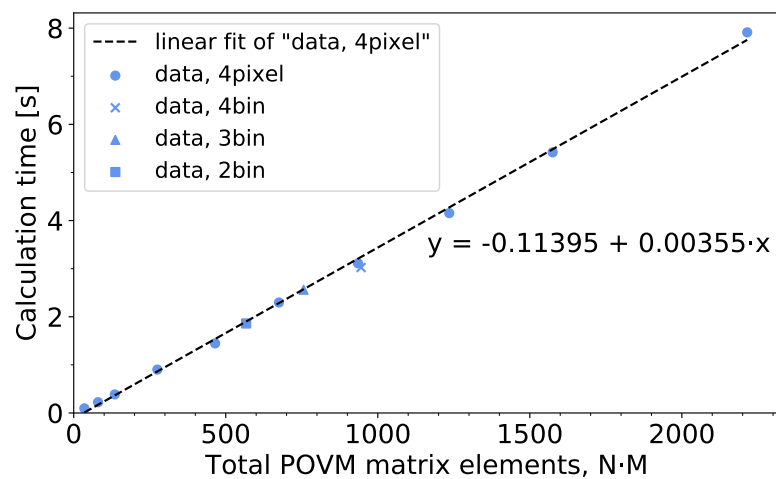


Figure A.2: Calculation time as a function of the total elements of the POVM matrix Π , $N \cdot M$. The linear fit is based on the data from Section 4.3.6, specifically the “truncated reconstructions” from Fig. 4.10. For the small sample size of ten data points a linear dependency can be observed. The calculation time for the reconstruction of the 4-bin detector from Section 5.2.3 and also for the adjusted 3-bin and 2-bin detectors do agree with the linear fit.

Tomographic Reconstruction Python Code

```

1 """
2 @author: Timon Schapeler
3 Based on MATLAB code from A. Feito (http://www.photonicquantum.info/Tools.html)
4 """
5 import cvxpy as cp
6 import numpy as np
7 def reconstruction(F, P, gamma):
8     """
9     Reconstruct the POVM elements based on the given F and P matrices.
10
11     Parameters
12     -----
13     F : np.array, DxM matrix
14     Coherent input state matrix, expanded in Fock basis up to M.
15     P : np.array, DxN matrix
16     Measurement statistics matrix.
17     gamma : float, between 0 and 1
18     Smoothing factor.
19
20     Returns
21     -----
22     reconstructed_POVMs : np.array, MxN matrix
23     Contains the reconstructed POVM elements of the detector.
24     """
25     # Get dimensions of the matrices
26     D, N = P.shape #number of probe states and detection outcomes
27     M = F.shape[1] #Hilbert space dimension
28     # Setup the variable with first constraint
29     rec_POVM = cp.Variable((M,N), nonneg=True) #nonneg ensures positive POVMs
30     # Setup smoothing
31     smooth = 0
32     for n in range(0,N):
33         for i in range(0,M-1):
34             smooth = smooth + (rec_POVM[i,n] - rec_POVM[i+1,n])**2
35     # Add the second constraint (summation to one for each row)
36     constraints_list = []
37     for i in range(M):
38         constraints_list.append(sum(rec_POVM[i,:]) == 1)
39     # Define objective and optimization problem
40     obj = cp.Minimize(cp.norm(P - F * rec_POVM, 'fro') + gamma*smooth)
41     problem = cp.Problem(obj, constraints = constraints_list)
42     # Solve the problem
43     problem.solve(solver=cp.SCS, verbose=True) #solvers: SCS, CVXOPT, ECOS
44     print("status:", problem.status) #print the status
45     print("optimal value", problem.value) #print the optimal value
46     #print("optimal var", rec_POVM.value) #print the optimal variable
47     reconstructed_POVMs = np.asarray(rec_POVM.value) #convert to np.array
48     np.save('rec_POVM_gamma' + str(gamma) + '.npy', reconstructed_POVMs)
49     return reconstructed_POVMs

```


Acknowledgements

First of all, I would like to thank Jun.-Prof. Dr. Tim J. Bartley for the opportunity to work in his group and for proposing the very interesting topic of quantum detector tomography as my project. I really enjoyed working on this topic. His help as my supervisor and the great discussions always lead to new thoughts which encourage and inspire me.

I would also like to thank Prof. Dr. Torsten Meier for investing his time in reading my thesis.

Especially, I would like to thank Jan Philipp Höpker for the great advice he provided at any time. Thanks as well for supporting me in the laboratory, all the interesting discussions and proofreading parts of my thesis.

I am also thankful to Vahid Ansari for initial tips about quantum detector tomography, Johannes Tiedau for general tips and Thomas Hummel for his advice and proofreading parts of my thesis.

Furthermore, I am grateful to all members of the Mesoscopic Quantum Optics Group for the enjoyable and friendly atmosphere in our office.

Finally, I would like to thank my friends and family for their support. Special thanks go to Nina Lange, as she is always there for me.

Erklärung

Ich versichere, dass ich die Arbeit ohne fremde Hilfe und ohne Benutzung anderer als der angegebenen Quellen angefertigt habe und dass die Arbeit in gleicher oder ähnlicher Form noch keiner anderen Prüfungsbehörde vorgelegen hat und von dieser als Teil einer Prüfungsleistung angenommen worden ist. Alle Ausführungen, die wörtlich oder sinngemäß übernommen worden sind, sind als solche gekennzeichnet.

Ort, Datum

Unterschrift